



DEPARTMENT OF APPLIED INFORMATICS  
FACULTY OF MATHEMATICS, PHYSICS AND INFORMATICS  
COMENIUS UNIVERSITY, BRATISLAVA, SLOVAKIA

---

# MEASUREMENT, RENDERING AND EDITING OF THE MATERIAL APPEARANCE

(Project of dissertation)

*Mgr. Andrej Mihálik*

I hereby declare that I worked on this report alone using only the referenced publications.

.....

# Abstract

Humans recognize objects visually on the basis of material composition as well as shape. In reality, appearance is controlled by the complex interplay of light (electromagnetic radiation coming from various sources) and the materials composing the objects in the scene, with complex scattering effects taking place all along the path of light. In computer graphics there are two fundamental visual attributes used to describe the appearance of objects in synthetic images. These attributes are color and gloss.

In this work we are attempting to overview fundamental knowledge of material appearance in field of computer graphics. We start with discussion of some aspects of the human perception of the light and outline some physical properties of the light-material interactions. Then we discuss fundamentals of the color perception and the colorimetry. We also overview common models of how materials scatter light. Then we introduce some system devoted to material appearance measurement.

In our research we are focusing on acquirement and analysis of the data related to the material appearance. These data explain how the material reflects the light and can be used to render synthetic images. We are also focusing on editing and transporting of the material appearance of objects depicted in single images.

# Contents

<b>1</b>	<b>Introduction</b>	<b>1</b>
1.1	Light and Human Visual System . . . . .	2
1.2	Light and Surface Interaction . . . . .	4
1.3	Project Outline . . . . .	5
<b>2</b>	<b>Color</b>	<b>6</b>
2.1	Standard Illuminants . . . . .	7
2.2	Color Spaces . . . . .	8
2.2.1	RGB Color Space . . . . .	10
2.2.2	L*a*b* Color Space . . . . .	12
<b>3</b>	<b>Reflectance Models</b>	<b>14</b>
3.1	Mathematical Background . . . . .	14
3.1.1	BRDF Properties . . . . .	17
3.2	Fresnel Reflectance . . . . .	18
3.3	Anisotropic Reflectance . . . . .	19
3.4	Lambertian Reflectance . . . . .	19
3.5	Phong Reflectance . . . . .	20
3.6	Ward Reflectance . . . . .	21
3.7	Cook-Torrance Reflectance . . . . .	22
3.7.1	Microfacet Distribution . . . . .	22
3.7.2	Cook-Torrance Model . . . . .	23
3.8	Psychophysically-Based Light Reflection Model . . . . .	24
<b>4</b>	<b>Measurement</b>	<b>26</b>
4.1	BRDF Measurement . . . . .	26
4.2	Industrial Measurement . . . . .	27
4.2.1	Virtual Glossmeter . . . . .	28
<b>5</b>	<b>Project of Dissertation</b>	<b>30</b>
5.1	Research Interests and Goals . . . . .	30
5.2	Solutions and Techniques . . . . .	31
5.2.1	Appearance editing . . . . .	31
5.2.2	Material appearance transfer from the object depicted in a image to another object . . . . .	31

---

5.2.3	Virtual goniospectrophotometer . . . . .	33
5.2.4	Measurement of gloss and albedo . . . . .	33
5.2.5	Sparkling analysis and rendering . . . . .	34
5.2.6	Rendering of the spectral effects . . . . .	34
<b>6</b>	<b>Preliminary Results</b>	<b>36</b>
6.1	Material appearance transfer between images . . . . .	36
6.1.1	Separation of the Specular Component . . . . .	36
6.1.2	Shape from Shading . . . . .	38
6.1.3	Transport of the Appearance . . . . .	38
6.1.4	Results . . . . .	40
	<b>Bibliography</b>	<b>43</b>
	<b>Publications</b>	<b>49</b>

# Chapter 1

## Introduction

The appearance of an object is important in both the real world and in a computer graphics scene. From an object's color alone we can determine the season by the leaves, the weather by the sky, or the food freshness. Gloss reveals to us the cleanliness of a table, or the age of a car, as we can see in Figure 1.1. These judgments are made instinctively by analyzing the light reflected from the items to our eyes. When applied to synthetic imaging, we judge the realism of a computer graphic picture by the appearance of the objects in the rendered environment. If the light that reaches us from the image evokes a visual response similar to that of viewing the real world scene, we describe the picture as being realistic.



**Figure 1.1:** A comparison of old and new car coat. Left: Rough surface of rusty car absorbs and scatters incident light [27]. Right: Smooth polished coating of new car reflects light source [68].

To acquire realistic appearance of scene objects, we need to know how they interact with incoming light. Visual appearance of them then depends on the light source, their geometry and chemistry, and also the human perception.

Although, we are focusing in this work mostly on physical light-material interaction, human perception and judgment how the object will look depends not only on physical phenomena, but also on psychological phenomena. Light leaving an object that reaches our eye is the physical stimulus that allows us to see it. The connection between that stimulus and the idea that we form about the object is a complex result of the physiology of human eye and the processing in the brain.

## 1.1 Light and Human Visual System

Light is the electromagnetic radiation. In the wavelength band between roughly 380 nm and 830 nm is light visible to the human eye. Wavelengths in this band represent colors from violet to red. All these colors forms visible spectrum. For example wavelength of the yellow light is about 570 nm. An object which reflects just light with this wavelength appears as yellow. However, if object reflects green (wavelength about 520nm) and red (wavelength more than 650nm) light of the same intensity ratio, this object appears also yellow. This is because retina of the human eye contains of three types of color receptors cells: short-wavelength cones, middle-wavelength cones and long-wavelength. Short-wavelength cones are responsive to light that is perceived as violet or blue. Middle-wavelength cones are responsive to yellow or green light and have negligible response to the light of the wavelength about 650nm. Long-wavelength cones are not as much responsible to green light as to yellow, but they have certain response to light of the wavelength about 650nm and more. Lower response of long-wavelength cones to green light is recompensed with presence of red light, and therefore a composition of green and red light is perceived as yellow.

Another type of the photoreceptors, called rods, exists at the retina. Rods are used when very little light is available. They are approximately 25 times more sensitive than cones and are responsible for vision from twilight illumination to very dark lighting conditions when color recognition is delimited.

Human eye is not equally sensitive to all wavelengths in the visible range. The sensitivity of human eyes over the visible range under well-lit conditions is given by the luminous efficiency function, which can be approximated by a bell-shaped curve peaking at 555 nm, see Figure 1.2. Such a curve is standardized by the Commission Internationale de l'Eclairage (CIE) and is known as the  $V(\lambda)$  curve, or CIE photopic luminous efficiency curve. This curve implies that in human observation blue light seems darker then green light.

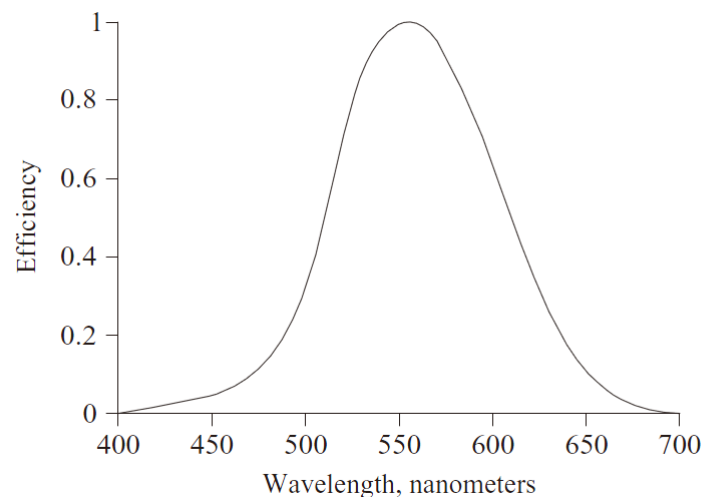


**Figure 1.2:** CIE standard observer photopic luminous efficiency curve [13].

The human visual system adapts to the prevailing conditions of illumination. Thus, adaptation renders visual system less sensitive in daylight and more sensitive at night. For example, car headlights that let drivers drive at night go largely unnoticed in daylight, as shown in Figure 1.3.

When we are for a while in dark and then our eyes are exposed to a brief light of moderately high intensity the response reaches its maximum and the photoreceptors are saturated. The photoreceptors lose sensitivity to any additional light intensity.



**Figure 1.3:** *Although the headlights are on in both images, our eyes are less sensitive to car headlights when background intensity is higher [64].*

Photoreceptors contain photopigment rhodopsin (composition of a protein called opsin and a chromophore derived from vitamin A known as retinal) in their outer segment. When rhodopsin is exposed to the light, then retinal changes shape and activates the protein called transducin. Each transducin then activates the enzyme cGMP-specific phosphodiesterase, which leads to closing a membrane bound cGMP-gated cation channels. Steady current flows through these channels into the photoreceptor, carried mainly by sodium cations, constituting a "dark current" that partially depolarizes the photoreceptor cell. When ions flow stops, photoreceptors charge inside the membrane becomes more negative (cell becomes hyperpolarized). This leads to the reduction in the release of the neurotransmitter glutamate, which affects membrane potential of the bipolar cells (cells between photoreceptors and neurons of the retina called ganglion cells). The neurons then relay the signal to the primary visual cortex which is located at the back of the brain.

The absorbance characteristics for the photopigments of the rods and cones are shown in Figure 1.4. Note that Figure 1.4 only shows relative sensitivity. Much higher sensitivity of rods than sensitivity of cones is due to the fact that rods have a larger diameter and are longer. Also, it takes longer for the rod pigments to regenerate.

Photochemical reactions discussed above breaks down photosensitive pigments and temporarily renders the rod and cone photoreceptors insensitive - a process called bleaching. The pigments are regenerated in a relatively slow process. Thus the visual adaptation as a function of light intensity could be attributed to the depletion and regeneration of photopigment. Rod photopigments are completely depleted when exposed to the higher light intensity.

However, cone photopigments are not significantly depleted even in bright sunlight. Although, the sensitivity of the cones continues to diminish according the prevailing conditions. This lack of correlation between photopigment concentration and visual sensitivity, as well as other experimental evidence, suggests that unless virtually all pigments are bleached the visual adaptation to different illumination conditions cannot be completely attributed to photo-pigment concentration [14].

Interesting property of human visual system is ability to recognize same color under different illuminants. For example, piece of paper illuminated by sun is perceived as white. Moreover, same paper is perceived by a human as white under yellow lamp, while depicted in photography is yellow. This is called color constancy [23, 82]. Nowadays cameras have feature which allows adjustment of colors under different illumination of scenes. This feature is called white balance.

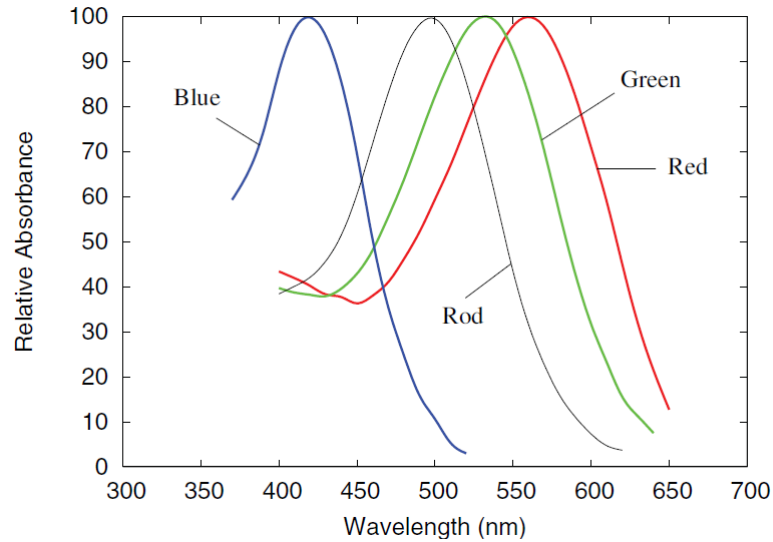


**Figure 1.4:** Absorbance characteristics for the photopigments found in the rods and cones. The maximum absorbance of the red, green, and blue cones is located at 559 nm, 531 nm, and 419 nm, respectively. The maximum absorbance of the rod is located at 496 nm [23].

## 1.2 Light and Surface Interaction

In geometric optics light is traveling along straight paths from the source. As ray of light hits surface, it may be either absorbed or redirected in a new direction. If light hits the surface, quantity of redirected light may decrease as a result of the absorption. Light of some wavelengths may be absorbed more than light of others, which turns out a color perception. Incident light may be also scattered into multiple directions. Scattered light which leaves a surface in each direction is an effect of the light interaction with rough surfaces [55]. If surface is perfectly polished, incident ray is redirected into its mirror image (angle of incidence is equal to the angle of reflection), although certain amount of incident light may be refracted into the material volume.

Reflection and refraction that occur at a material boundary, are described by the Fresnel equations as a function of the angle of incidence. Many materials exhibit a higher degree of reflectivity at extremely shallow (grazing) angles. This phenomenon is notable when we are looking at a water surface, see Figure 1.5. If we are above water and looking at the water surface at a grazing angle, we will see a specular (mirrorlike) reflection of a bank. At steeper angles we will see a lake bottom rather than the sky above.

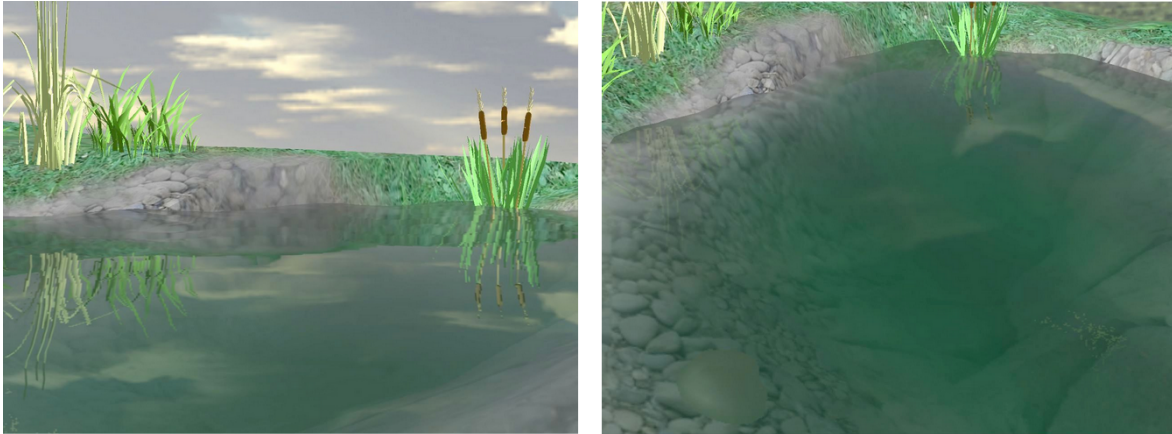


**Figure 1.5:** Example of the Fresnel phenomenon. Left: Reflection at the water surface. Right: Refraction of the bottom [49].

### 1.3 Project Outline

- **Chapter 1** (*Introduction*) We introduce some functionality of a human visual system. We will reveal some aspects of the human perception of the light and outline some physical properties of the light-material interactions.
- **Chapter 2** (*Color*) In this chapter we introduce some knowledges gained by the field of science called colorimetry. We will discuss some wavelength dependent properties of the light. We will also briefly overview some important color spaces.
- **Chapter 3** (*Reflectance Models*) This chapter is devoted to the mathematical descriptions of the common models for how materials scatter light. We will define the basic terms, concepts, and notations used in describing light and materials.
- **Chapter 4** (*Measurement*) In this chapter we overview systems for measuring BRDF. This chapter also introduces some industrial measurement devices.
- **Chapter 5** (*Project of Dissertation*) This chapter reveals intentions in our ongoing research and state desired goals we want to achieve in the future.
- **Chapter 6** (*Preliminary Results*) Finally we conclude with our preliminary results, showing a method for material appearance transport between single images.

## Chapter 2

# Color

If ray of the white light hits triangular prism, light breaks up into its constituent spectral colors, see Figure 2.1. In 17's century people believed that light is colorless, and that the prism itself produced the color. This image was changed by Isaac Newton and his experiments. He passed the red color created by one prism through a second prism and found the color unchanged. From this, he concluded that the colors must already be present in the incoming light thus, the prism did not create colors, but merely separated colors that are already there. He also used a lens and a second prism to recompose the spectrum back into white light.

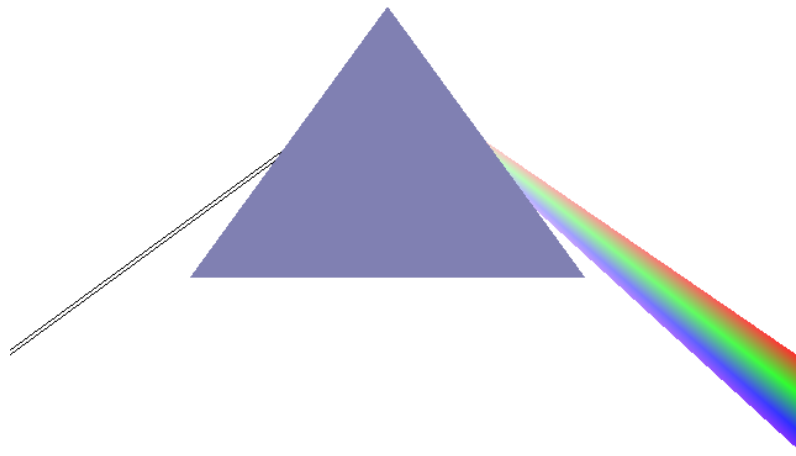


**Figure 2.1:** *Braking light into spectrum by the prism.*

Speed of light  $c$  is 299,792,458 m/s in the vacuum. As light travels through matter, it is gradually absorbed and emitted by atoms in its path. These processes consume certain amount of time and it causes that light appears to travel slower. This slower speed  $v$  depends both on the type of the matter and the wavelength of light.

A measure of how much the velocity of a wave is reduced inside a medium is called index of refraction. Index of refraction  $n$  is defined by the following formula:

$$n = \frac{c}{v}. \quad (2.1)$$

When light traveling in one transparent medium encounters a boundary with a second transparent medium, a portion of the light is reflected and a portion is transmitted into

the second medium. As the transmitted light moves into the second medium, it changes its direction of travel; that is, it is refracted, see Figure 2.2. The law of refraction, also known as Snell's law, describes the relationship between the angle of incidence  $\theta_i$  and the angle of refraction  $\theta_t$ , in mathematical terms:

$$\frac{\sin\theta_i}{\sin\theta_t} = \frac{n_2}{n_1}, \quad (2.2)$$

where  $n_1$  and  $n_2$  are the index of refraction of the first and second media, respectively. Because the index of refraction depends on the light wavelength, the medium refracts lights with different wavelengths to different directions. Therefore the prism decomposes light which consists of all visible wavelengths into the visible spectrum.

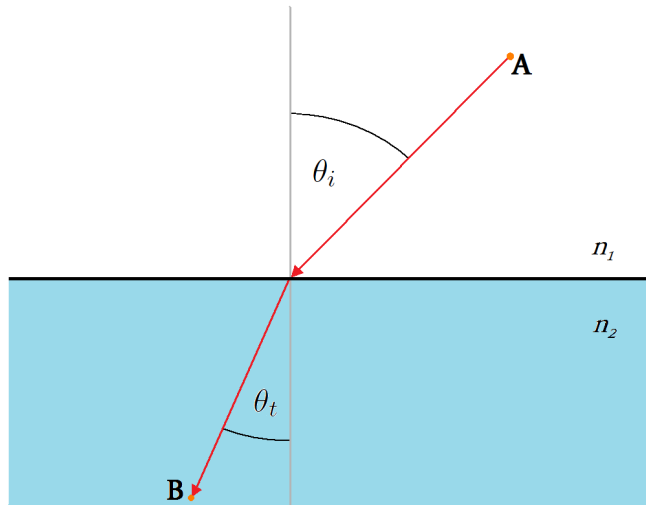


**Figure 2.2:** Light changes its trajectory at the border between media because it travels the path which takes the least time rather than shortest path. If light would be traveling straight from A to B, then it would spend more time in slower media.

## 2.1 Standard Illuminants

Light sources are described by their *spectral power distribution* (SPD). SPD is a representation of the radiant power emitted by a light source as a function of wavelength.

The International Commission on Illumination has defined a set of standard illuminants to be used for colorimetry. Figure 2.3 shows SPD of the CIE illuminants  $D_{55}$ ,  $D_{65}$ , and  $D_{75}$ . Illuminant  $D_{65}$  represents the noon daylight with a correlated color temperature of approximately 6500 K. Illuminant  $D_{55}$  with correlated color temperatures of approximately 5500 K represents the mid-morning. Illuminant  $D_{75}$  with correlated color temperatures of approximately 7500 K represents the north sky daylight. The color temperature of a light is the temperature of an ideal black-body radiator that radiates light of comparable hue to that light [36]. Higher color temperatures (5000 K or more) are cool (blueish white) colors; lower color temperatures (2700 - 3000 K) are warm (yellowish white through red) colors.

A blackbody radiator is experimentally realized by creating a concavity whose walls are kept at a constant temperature. Radiation can only escape through a little hole. The hole has to be so small that radiation entering or leaving the whole does not alter the temperature of the black-body radiator. Radiation is measured in front of the hole using a spectrometer. SPD of a black-body depends only on its temperature. It is given off equally in all directions. Such a radiator which emits radiation equally in all directions is called a *Lambertian radiator*.

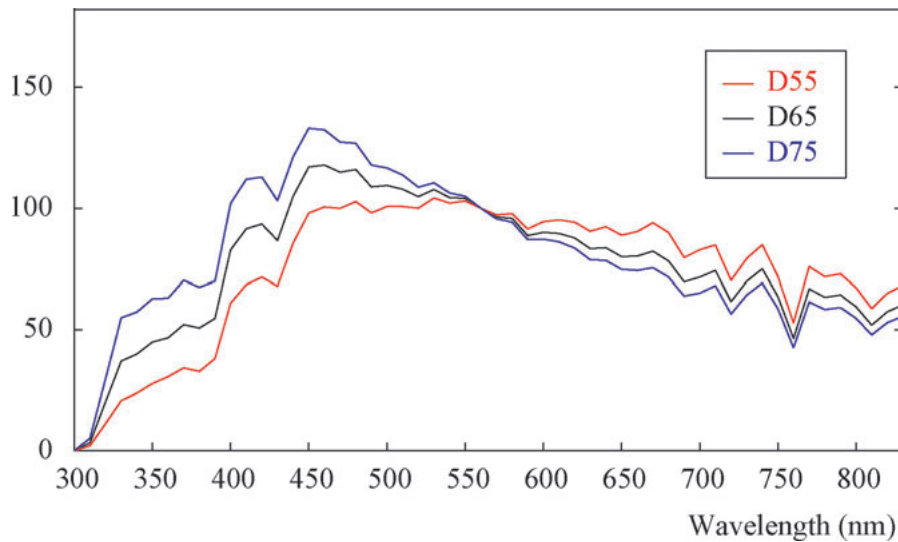


**Figure 2.3:** Spectral power distribution of CIE illuminants [64].

## 2.2 Color Spaces

As mentioned in chapter 1, there are three types of photoreceptor cells in the human eye responsible for the color vision. Short-wavelength cones are most sensitive to blue light, middle-wavelength to green light and long-wavelength to red light. Absorbance curves of these three types of cones are in Figure 1.4. This indicates that other colors could be created by using just three colors.

Multiple colormatching experiments have been performed to match colors from visible spectrum to the colors created by three primary light sources. In these experiments, primary light sources have been projected to one side of a white screen. A fourth light source, the target color which represents a sample color from spectrum, have been projected to the other side of the screen. Participants in the experiments were given control over the intensity of each of the three primary light sources and were asked to match the target color. By recording the intensities of the three primaries for each target wavelength, three color-matching functions have been obtained:  $\bar{r}(\lambda)$ ,  $\bar{g}(\lambda)$  and  $\bar{b}(\lambda)$ . Figure 2.4 shows weights for primary lights at wavelengths 700 nm, 546.1 nm, and 435.8 nm to match a color stimulus of a given wavelength. Note that the red curve gains negative values. As the light source can not radiate negative intensities, negative values of the red primary source was obtained in the experiment, by adding red light to the target color. Because the red cones have plumbless response to the green light at wavelength 546.1 nm, the negative values of the red light are required to form colors from the band of the spectrum between blue and green . These negative values are caused by the fact, that to certain wavelengths, more than just one type of cones has a response. This problem implies that not every visible color is able to construct from red, green and blue light.

In that it is simpler to deal with a color space whose values are always positive, the CIE has defined alternative color-matching functions chosen such that any color may be matched with positive primary coefficients. These color-matching functions are named  $\bar{x}(\lambda)$ ,  $\bar{y}(\lambda)$  and  $\bar{z}(\lambda)$  (see Figure 2.5). These weights are obtained by two steps. Firstly, following linear

transformation is applied:

$$\begin{bmatrix} x(\lambda) \\ y(\lambda) \\ z(\lambda) \end{bmatrix} = \begin{bmatrix} 0.49000 & 0.31000 & 0.20000 \\ 0.17697 & 0.81240 & 0.01063 \\ 0.00000 & 0.01000 & 0.99000 \end{bmatrix} \begin{bmatrix} \bar{r}(\lambda) \\ \bar{g}(\lambda) \\ \bar{b}(\lambda) \end{bmatrix} \quad (2.3)$$

and after the linear transformation has been applied, the weights  $\bar{x}(\lambda)$ ,  $\bar{y}(\lambda)$  and  $\bar{z}(\lambda)$  are computed as follows:

$$\bar{x}(\lambda) = \frac{x(\lambda)}{y(\lambda)} V(\lambda) \quad (2.4)$$

$$\bar{y}(\lambda) = V(\lambda) \quad (2.5)$$

$$\bar{z}(\lambda) = \frac{z(\lambda)}{y(\lambda)} V(\lambda) \quad (2.6)$$

where  $V(\lambda)$  is the photopic luminous efficiency function shown in Figure 1.2.

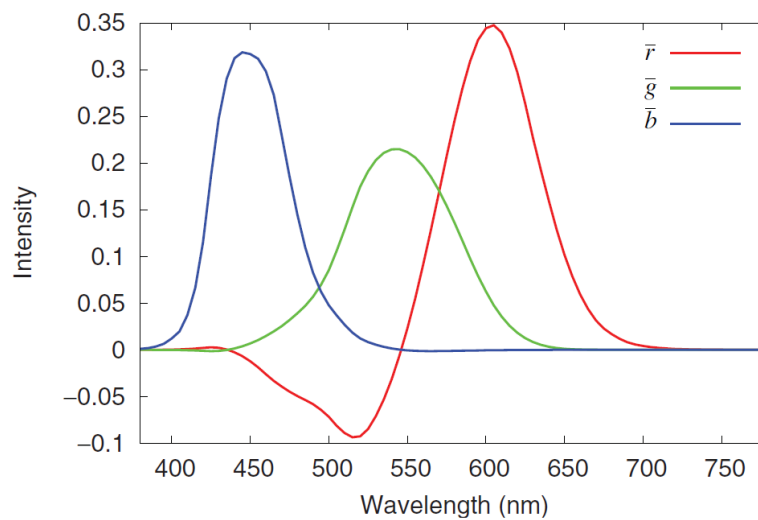


**Figure 2.4:** Intensities for red, green and blue light to create a color of a given wavelength [23].

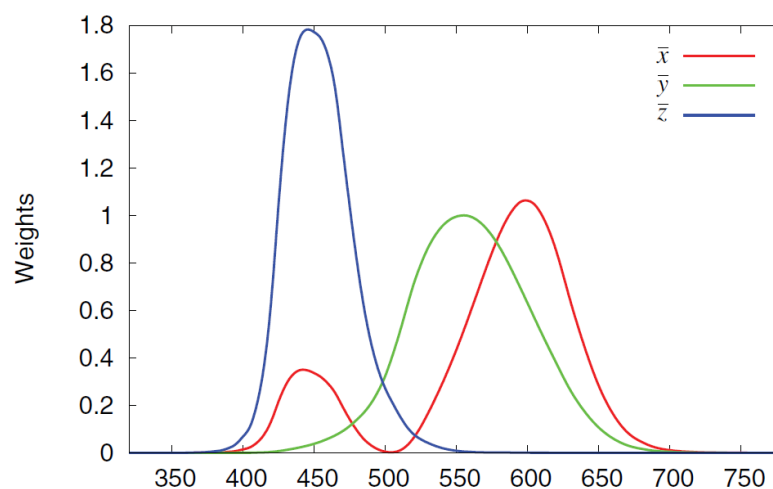


**Figure 2.5:** Nonnegative weights used by a standard observer to create any given color sensation [23].

CIE has defined tristimulus values  $X$ ,  $Y$ , and  $Z$ . These values represent imaginary over-saturated colors [69], thus illumination  $Q_\lambda$  of every color from the visible spectrum can be represented by the following linear combination

$$Q_\lambda = \bar{x}(\lambda)L_X + \bar{y}(\lambda)L_Y + \bar{z}(\lambda)L_Z, \quad (2.7)$$

where  $L_X$ ,  $L_Y$  and  $L_Z$  are primary lights which emit light of imaginary colors corresponding to  $X$ ,  $Y$  and  $Z$ , respectively. Tristimulus values of the CIE XYZ color space are mathematically obtained by integration of the illumination  $Q_\lambda$  through all color from the visible spectrum.

$$X = \int_{380}^{830} Q_\lambda \bar{x}(\lambda) d\lambda \quad (2.8)$$

$$Y = \int_{380}^{830} Q_\lambda \bar{y}(\lambda) d\lambda \quad (2.9)$$

$$Z = \int_{380}^{830} Q_\lambda \bar{z}(\lambda) d\lambda \quad (2.10)$$

The CIE XYZ matching functions are defined such that a theoretical equal-energy stimulus, which would have unit radiant power at all wavelengths, maps to tristimulus value (1, 1, 1). Further, note that  $\bar{y}(\lambda)$  is equal to  $V(\lambda)$  - another intentional choice by the CIE. Thus,  $Y$  represents photometrically weighted quantities.

For any visible color, the tristimulus values in the CIE XYZ color space are all positive. However, as a result the CIE primaries are not realizable by any physical device.

If the energy of each primary color is increased by the same percentage, then the relative responses of the receptors will not be any different. Therefore, colors are usually specified using normalized colors, or chromaticities. The chromaticities of the CIE XYZ color space are given by

$$x = \frac{X}{X + Y + Z} \quad (2.11)$$

$$y = \frac{Y}{X + Y + Z} \quad (2.12)$$

$$z = \frac{Z}{X + Y + Z} = 1 - x - y \quad (2.13)$$

Because  $z$  is known if  $x$  and  $y$  are known, only the latter two chromaticity coordinates need to be kept. Chromaticities are relative, which means that within a given system of primary stimuli two colors with the same relative spectral power distribution will map to the same chromaticity coordinates.

Chromaticity coordinates may be plotted in a chromaticity diagram with two axes. A CIE  $xy$  chromaticity diagram is shown in Figure 2.6. All monochromatic wavelengths map to a position along the curved boundary, called the spectral locus, which is of horseshoe shape.

The three primaries used for any given color space will map to three points in a chromaticity diagram and thus span a triangle. This triangle contains the range of colors that may be represented by these primaries (assuming nonnegative tristimulus values). The range of realizable colors given a set of primaries is called the color gamut. Colors that are not representable in a given color space are called out-of-gamut colors, see Figure 2.7.

### 2.2.1 RGB Color Space

Color spaces encompass two different concepts. First, they are represented by a set of formulas that define a relationship between a color vector (or triplet) and the standard CIE XYZ color space. This is most often given in the form of a 3-by-3 color transformation matrix, although

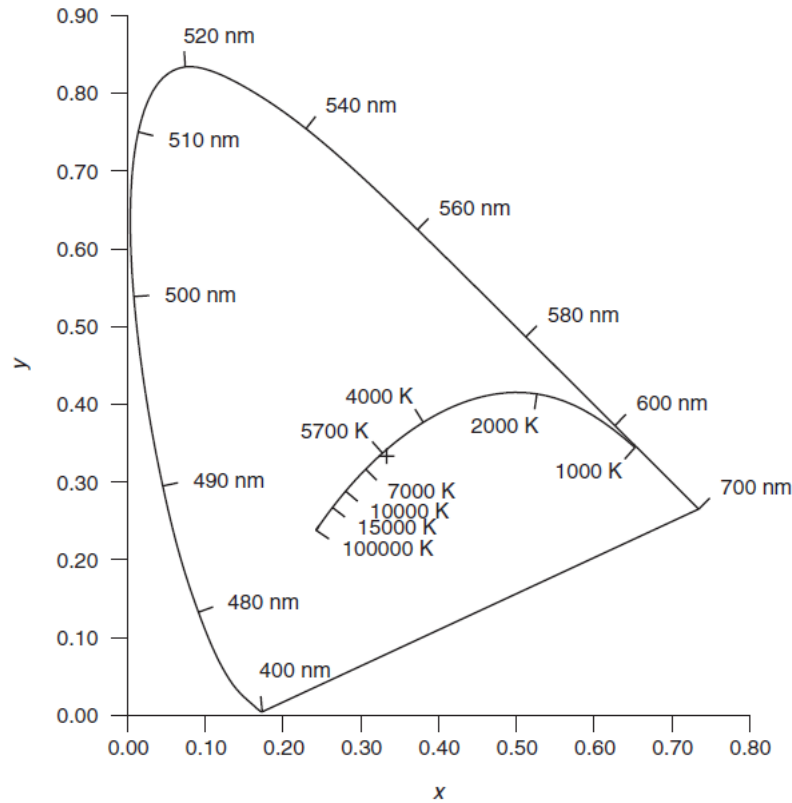


**Figure 2.6:** Gamut of colors in CIE XYZ space. The chromaticities of light in the visible range from 400 nm to 700 nm form a horseshoe-shaped region. The chromaticities for a black-body radiator at different temperatures is shown in the center. The color of a blackbody radiator passes from red at low temperatures through white and on to blue at higher temperatures. The point of equal energy is located at the center of the graph [23].

there are additional formulas if the space is nonlinear (e.g. CIE LAB). Second, a color space is a 2D boundary on the volume defined by this vector, usually determined by the minimum and maximum value of each primary - the color gamut.

In the RGB color space, color is defined with respect to a unit cube [28]. The cube is defined using three axes, red, green, and blue, as shown in Figure 2.8. Each point inside the cube defines a unique color. Let  $c = [R, G, B]$  with  $R, G, B \in [0, 1]$  be a point inside the color cube. Then the individual components  $r, g, b$  specify the intensity of the red, green, and blue components that are used to produce a single pixel on the screen. The eight corners of the cube can be labeled with the colors black, red, green, blue, yellow, magenta, cyan, and white. The gray scale is located inside the cube. It starts at the origin with the black color and extends all the way through the cube to the opposite corner of the cube to the white color.

The conversion from XYZ to RGB may be computed by the following linear transformation:

$$\begin{bmatrix} R \\ G \\ B \end{bmatrix} = \begin{bmatrix} 3.2405 & -1.5371 & -0.4985 \\ -0.9693 & 1.8760 & 0.0416 \\ 0.0556 & -0.2040 & 1.0572 \end{bmatrix} \begin{bmatrix} X \\ Y \\ Z \end{bmatrix} \quad (2.14)$$

As wavelength responses of red and green cones are noticeably overlapping and we can not obtain negative intensities of the red light, the gamut of this space does not involve all visible colors. Nevertheless, the gamut of the following color space consists of all visible colors.

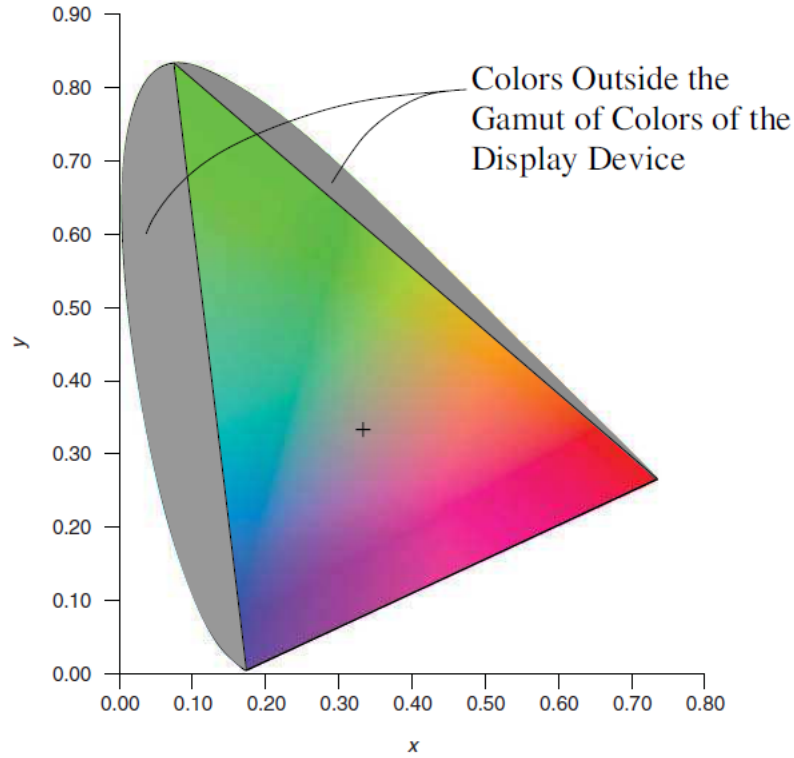


**Figure 2.7:** If three monochromatic primary colors are chosen for the display device then some colors cannot be created by the display device. The triangular-shaped subregion assumes three monochromatic primary colors at 400 nm, 520 nm, and 700 nm. Colors that are located inside the two gray regions lie outside the gamut of colors of the display device [23].

### 2.2.2 $L^*a^*b^*$ Color Space

The CIE LAB color space is a three-dimensional color space that is perceptually more uniform than the CIE XYZ color space. This color space was intended for use with surface colors. The three coordinates  $L^*$ ,  $a^*$ , and  $b^*$  are computed from the tristimulus values X, Y, and Z as follows:

$$L^* = \begin{cases} 116\left(\frac{Y}{Y_n}\right)^{\frac{1}{3}} - 16 & \text{if } \frac{Y}{Y_n} > 0.008856 \\ 903.3\left(\frac{Y}{Y_n}\right) & \text{if } \frac{Y}{Y_n} \leq 0.008856 \end{cases} \quad (2.15)$$

$$a^* = 500\left(f\left(\frac{X}{X_n}\right) - f\left(\frac{Y}{Y_n}\right)\right) \quad (2.16)$$

$$b^* = 200\left(f\left(\frac{Y}{Y_n}\right) - f\left(\frac{Z}{Z_n}\right)\right) \quad (2.17)$$

where  $X_n$ ,  $Y_n$ , and  $Z_n$  describe a specified white object color stimulus and the function  $f$  is defined as

$$f(x) = \begin{cases} x^{\frac{1}{3}} & \text{if } x > 0.008856 \\ 7.787x + \frac{16}{116} & \text{if } x \leq 0.008856 \end{cases} \quad (2.18)$$

$L^*$  describes lightness and extends from 0 (black) to 100 (white).

Chromatic components  $a^*$  and  $b^*$  are based on the opponent process. It is a process of coding colors in neural system. The three types of cones have some overlap in the wavelengths of light to which they respond, so it is more efficient for the visual system to record differences between the responses of cones, rather than each type of cone's individual response. The

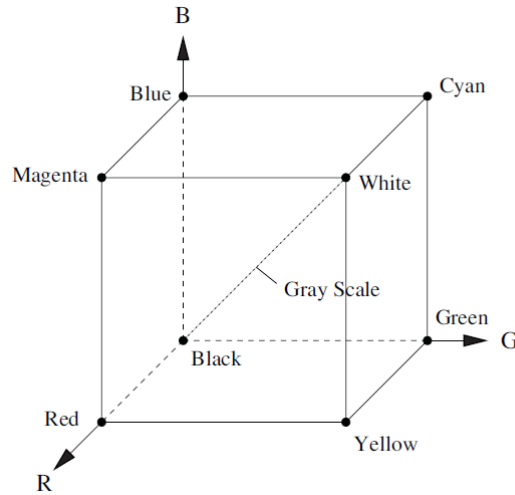


**Figure 2.8:** RGB color space. Color is defined with respect to a unit cube [23].

opponent color theory suggests that there are three opponent channels: red versus green, blue versus yellow, and black versus white (the latter type is achromatic and detects lightness). Therefore  $a^*$  denotes position between red and green, and negative values of  $a^*$  indicate green while positive values indicate magenta. Coordinate  $b^*$  denotes position between yellow and blue and, negative values of  $b^*$  indicate blue. Positive values of  $b^*$  indicate yellow.

Uniform changes of components in the CIE LAB color space aim to correspond to uniform changes in perceived color, so the relative perceptual differences between any two colors in CIE LAB can be approximated by treating each color as a point in a three dimensional space (with three components:  $L^*$ ,  $a^*$ ,  $b^*$ ) and taking the Euclidean distance between them.

The main advantage of this color system is that color is decoupled from intensity. For instance, if we view a red sphere illuminated by a single light source, then illumination varies over the surface of the sphere (Figure 2.9). Because of this, one can use this information to extract the three-dimensional shape of objects given a single image. This research area is known as *shape from shading* [33, 2, 66, 34, 40]. But suppose we wanted to segment the image. We want to locate all pixels that belong to the sphere. This can be easily done using a color space where color is specified by lightness, saturation, and hue. Knowing that the sphere is red, one transforms the RGB values into such a color space. All pixels that have a red hue are assumed to belong to the sphere.

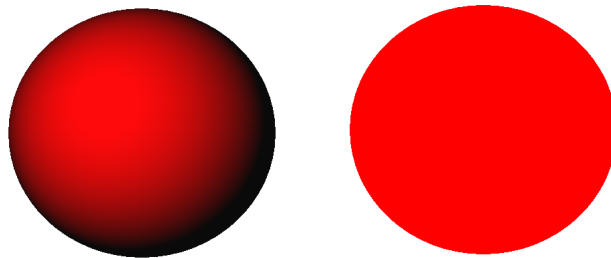


**Figure 2.9:** Left: Sphere illuminated by a single light source. Right: Segmentation is simpler if only hue is considered.

# Chapter 3

## Reflectance Models

The rendering of realistic images in computer graphics requires models of how objects reflect light [31]. Given a light source, a surface, and an observer, a reflectance model describes the intensity and spectral composition of the reflected light reaching the observer. The intensity of the reflected light is determined by the intensity and size of the light source and by the reflecting ability and surface properties of the material. The spectral composition of the reflected light is determined by the spectral composition of the light source and the wavelength-selective reflection of the surface. In this chapter we will discuss some models that try to mimic the appearance of real-world materials. But first in following section, we introduce some basic terms and definitions.

### 3.1 Mathematical Background

To make physically-based numerical definitions, we need to define various expressions for how incident light energy is distributed by a material with respect to position, direction, and wavelength. We need a mathematical mechanism that allows us to specify particular direction, position, or wavelength values, and then lets us add up all the particular values for all directions, positions, or wavelengths. We will rely that we can divide the quantities we are interested in into infinitesimally small pieces, which approach zero in size but still have meaning. We can take ratios of them to specify values at particular points. We can add up the small pieces at all points to find the quantity for the object as a whole.

Expressing directional variation introduces complications in addition to the concept of using infinitesimals. However, directional variations are essential to modeling appearance. The key quantity in defining light transfer in a particular direction is radiance. The key quantity for expressing the directional effect of materials on the incident radiance is the bidirectional reflectance distribution function (BRDF).

We denote energy as  $Q$ . The unit of energy is joule. Since we are interested in light transfer and not in its storage, we will only be dealing with the rate that it moves through an environment per unit time. The rate of energy transfer per second is power. The unit of power is watt. The power radiated is referred to as the radiant flux. To express the average flux  $\Phi$  over a period of time, we would measure the energy  $\Delta Q$  transferred through some time period  $\Delta t$  and find:

$$\Phi = \frac{\Delta Q}{\Delta t}. \quad (3.1)$$

To find the flux  $\Phi(t)$  at a particular instant, we consider differential period of time  $dt$ , which is the quantity  $\Delta t$  as it approaches zero. The differential amount of energy  $dQ$  transferred in  $dt$  is:

$$\Phi(t) = \frac{dQ}{dt}. \quad (3.2)$$

The average flux leaving per unit area (Figure 3.1), or radiant exitance  $M$ , is the total flux leaving divided by surface area  $A$ , or

$$M = \frac{\Phi}{A}. \quad (3.3)$$

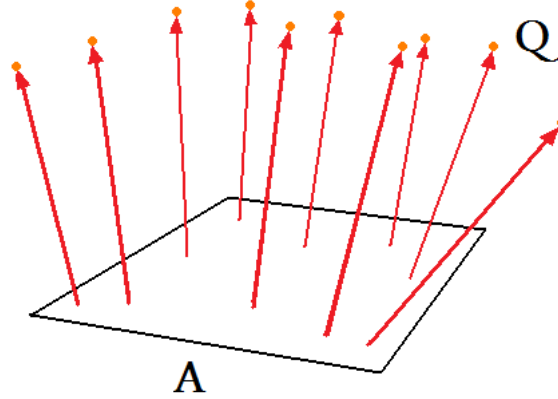


**Figure 3.1:** A quantum of the energy radiated from certain area per second.

To express the radiant exitance from a particular point  $(x, y)$  of the area, consider area around this particular point, which is shrinking until it is infinitesimally small. By considering this infinitesimally small area  $dA$ , we can define the radiant exitance  $M(x, y)$  at a particular position:

$$M(x, y) = \frac{d\Phi(x, y)}{dA}. \quad (3.4)$$

This denotes the energy of light emitted from the point at coordinates  $(x, y)$  per second per unit area. Which is fragment of energy  $d\Phi(x, y)$  emitted from infinitesimally small fragment of surface around  $(x, y)$  per fragment of time per infinitesimally small area  $dA$ .

The radiant energy per unit time and area arriving at a surface is called the *irradiance*  $E$ . It is defined in the same manner as  $M$ , with the only difference being whether the radiant energy is approaching or leaving the surface.

To include directional effects, we should consider how the point of view affects perception of an area. When viewing direction is perpendicular to a patch then perceived area of this patch is greater than perceived area of a patch viewed at a more glancing angle, see Figure 3.2. Since we are dealing with infinitesimally small patches then, we can omit perspective deformation. Therefore the value of reduced area can be computed using orthogonal projection. Such projection is achieved by multiplication of the area by  $\cos \theta$ .

The key quantity radiance in a particular direction  $\Theta$  is defined as the radiant flux per unit solid angle and unit area projected in the direction  $\theta$  (angle between surface normal and direction  $\Theta$ ). The radiance  $L$  is defined as:

$$L(x, y, \Theta) = \frac{dd\Phi(x, y, \Theta)}{\cos \theta dA d\omega}, \quad (3.5)$$

where  $d\omega$  is the solid angle. Solid angle is equal to the area of the segment of unit sphere. A solid angle equals the area of a segment of unit sphere in the same way a planar angle equals the length of an arc of unit circle.

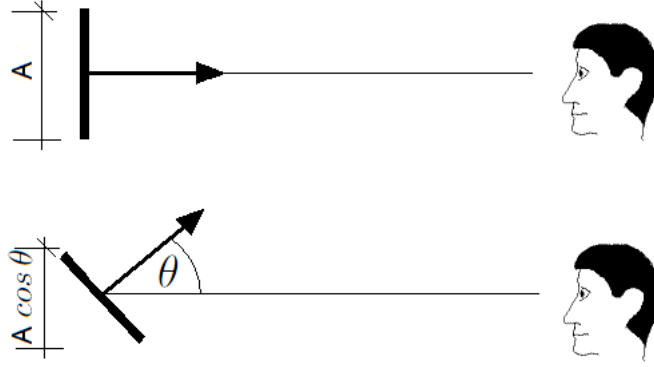


**Figure 3.2:** The apparent size of surface  $A$  is larger when it is projected in the direction of its surface normal, than when it is projected in a direction at an angle  $\theta$  to the normal.

The flux  $dd\Phi(x, y, \Theta)$  is a fragment of flux  $d\Phi(x, y)$  emitted from infinitesimally small patch at  $(x, y)$ , which exits unit sphere through the solid angle  $d\omega$  in the direction  $\Theta$ , see Figure 3.3. Although rays emitted from a patch to an area of the solid angle may have not particular direction, when patch and solid angle become infinitesimally small, only rays from patch with the specific direction reach the area of the solid angle.

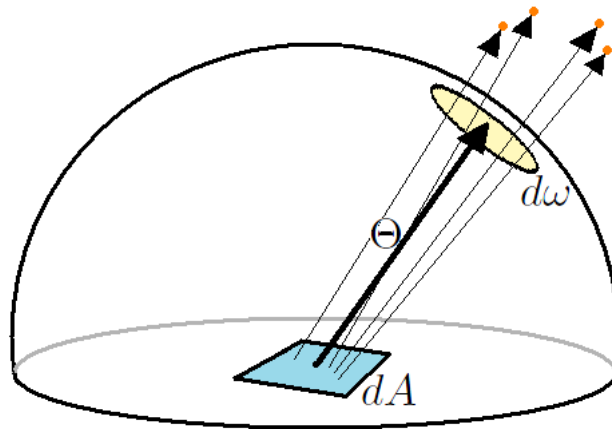


**Figure 3.3:** Flux of the light emitted from the area  $dA$  exiting unit sphere through solid angle.

The other variable that we want to account for in addition to time, position, and direction, is wavelength. Implicitly, since we are concerned with visible light in the span of 380 to 780 nm, all of the quantities we have discussed so far are for energy in that band. To express flux, irradiance, radiant exitance, intensity, or radiance as a function of wavelength, we consider the quantity at a value of  $\lambda$  within a small band of wavelengths between  $\lambda$  and  $\lambda + d\lambda$ . By associating a  $d\lambda$  with each value, we can integrate spectral values over the whole spectrum. We express the spectral quantities such as the spectral radiance as:

$$L(\lambda, x, y, \Theta) = \frac{ddd\Phi(\lambda, x, y, \Theta)}{\cos \theta dA d\omega d\lambda}. \quad (3.6)$$

To describe how a surface redirects light, we consider light incident on the surface at  $\mathbf{x} = (x, y)$  with radiance  $L(\lambda, \mathbf{x} \leftarrow \Theta_i)$  within a differential solid angle  $d\omega_i$ . The irradiance  $dE_i$  on the surface that will be either absorbed or redirected is:

$$dE_i(\lambda, \mathbf{x} \leftarrow \Theta_i) = L(\lambda, \mathbf{x} \leftarrow \Theta_i) \cos \theta_i d\omega_i. \quad (3.7)$$

The  $\cos \theta_i$  term appears because the radiance  $L$  measures energy per unit area  $dA$  in the direction of travel  $\Theta_i$ , and that direction projected into the orientation of the surface we are considering is  $\cos \theta_i dA$ . The  $d\omega_i$  term enters in because we want to know the effect of energy coming from a single direction representing a differential section of all the possible directions above the surface. The light reflected by the surface in each direction can be described by the radiance in each direction. The effect of a material redirecting light is then given by a function that is the ratio of the radiance reflected in a particular direction  $\Theta_r$  as a result of the total incident flux per unit area from another direction  $\Theta_i$  as shown in Figure 3.4. This ratio is referred to as the BRDF. It is defined by  $fr$ :

$$f_r(\lambda, \mathbf{x}, \Theta_i \rightarrow \Theta_r) = \frac{dL_r(\lambda, \mathbf{x} \rightarrow \Theta_r)}{dE_i(\lambda, \mathbf{x} \leftarrow \Theta_i)}. \quad (3.8)$$

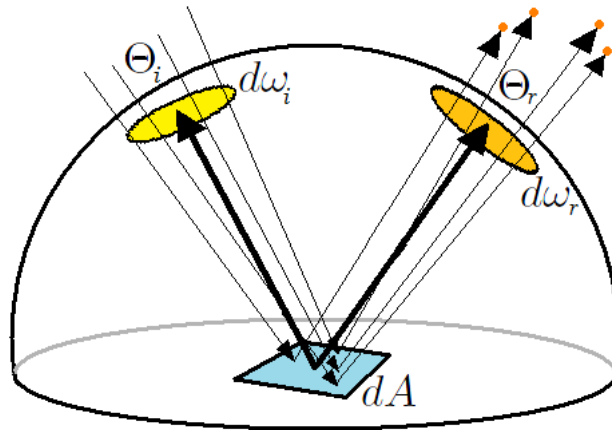


**Figure 3.4:** Flux of the light entered unit sphere through  $d\omega_i$  and reflected from the area  $dA$  through solid angle  $d\omega_r$ .

Note that fragment of the flux emerged in numerator of  $fr$  is fragment of the flux of the light of the wavelength band between  $\lambda$  and  $\lambda + d\lambda$ , which enters unit sphere through  $d\omega_i$ , is reflected from  $dA$  and leaves unit sphere through  $d\omega_r$ . While in denominator is emerged flux of the light of the wavelength band between  $\lambda$  and  $\lambda + d\lambda$ , which enters unit sphere through  $d\omega_i$  and is just incident with  $dA$ .

The BRDF is a distribution function, not a reflectance. It describes how the radiance is distributed in different directions, rather than expressing the fraction of energy reflected. If we would characterize the distribution of the light as the ratio of the reflected radiance and the incident radiance, then as solid angle  $d\omega_i$  approaches zero, the reflected radiance approaches also zero because less flux is incoming through  $d\omega_i$ . However, ratio of the reflected radiance and incident solid angle  $d\omega_i$  does not go to zero even if this solid angle approaches zero.

### 3.1.1 BRDF Properties

**Reciprocity:** Interchanging incoming and outgoing direction does not change the value of the BRDF:

$$f_r(\lambda, \mathbf{x}, \Theta_i \rightarrow \Theta_r) = f_r(\lambda, \mathbf{x}, \Theta_r \rightarrow \Theta_i). \quad (3.9)$$

This property is also known as *Helmholtz reciprocity* or *Helmholtz symmetry* and especially important for physically-based rendering algorithms like bidirectional path tracing. The results of some experiments have appeared to show a failure of the reciprocity relationship,

although such failures have subsequently been found to be due to measurement errors. Theoretical analysis and careful experiments on everyday materials have confirmed the validity of the reciprocity of the BRDF [74].

**Energy conservation:** The fraction of the energy reflected to all directions from light incident from one direction must be between 0 and 1 if the surface is not emitting light.

$$\int_{\omega_r} f_r(\lambda, \mathbf{x}, \Theta_i \rightarrow \Theta_r) \cos \theta_r d\omega_r \leq 1 \quad (3.10)$$

This property is most important for physically-based rendering algorithms that compute multiple bounces of light (e.g. Radiosity).

## 3.2 Fresnel Reflectance

Some shading models use Fresnel reflectance in their formulas. The Fresnel equations describe the amount of light is reflected and refracted at a perfectly smooth surface between two media.

The equations stem from wave optics and polarization of light has to be considered. Key components of the Fresnel equations are the reflection coefficient (usually denoted  $F_r$  in computer graphics), which gives the fraction of incident light that is reflected and the transmission coefficient  $F_t$ , which gives the fraction that is refracted. For parallel polarized light (p-polarized, the electric field oscillates in the plane of incidence) reflection coefficient is defined as:

$$r_{\parallel} = \frac{n_2 \cos \theta_i - n_1 \cos \theta_t}{n_2 \cos \theta_i + n_1 \cos \theta_t}. \quad (3.11)$$

For perpendicular polarized light (s-polarized, electric field perpendicular to plane of incident) it is:

$$r_{\perp} = \frac{n_1 \cos \theta_i - n_2 \cos \theta_t}{n_1 \cos \theta_i + n_2 \cos \theta_t}. \quad (3.12)$$

Here  $\theta_i$  and  $\theta_t$  are the angles between the surface normal and the directions of the incident and transmitted beams, and  $n_1$  and  $n_2$  are the indices of refraction of the media on the incident and transmitted side of the surface, see Figure 2.2.

Note that  $r_{\parallel}$  and  $r_{\perp}$  describe the relationship between the amplitudes of the involved electric fields. To get from the coefficients of an electric field strength to coefficients for an energy (or intensity, for that matter), we need to square them. For unpolarized light the reflection coefficient is

$$F_r = \frac{r_{\parallel}^2 + r_{\perp}^2}{2}. \quad (3.13)$$

The transmission coefficient is then

$$F_t = 1 - F_r. \quad (3.14)$$

Real materials are not perfect insulators. Therefore their index of refraction incorporates extinction coefficient  $k$ , which indicates the amount of absorption loss when the electromagnetic wave propagates through the material. Thus index of refraction can be written in complex form:

$$\hat{n} = n + ik, \quad (3.15)$$

where  $n$  is the refractive index indicating the phase velocity as in equation 2.1.

If  $n$  and  $k$  are unknown, but reflectance under  $\theta_i = 0$  is known, Cook & Torrance suggest to set  $k$  equal to 0 and compute  $n$  by:

$$n = \frac{1 + \sqrt{F_0}}{1 - \sqrt{F_0}}, \quad (3.16)$$

where  $F_0$  is Fresnel reflectance where  $\theta_i = 0$ . In paper [9] is derived Fresnel equation where  $k = 0$ . This procedure yields the correct value of  $F_r$  for normal incidence and a good estimate of its angular dependence, which is only weakly dependent on the extinction coefficient  $k$ .

### 3.3 Anisotropic Reflectance

Almost all materials exhibit some amount of anisotropy, meaning that their surfaces change in appearance as they are rotated about their surface normal. An extreme example of an anisotropic material is brushed metal. However, there are many materials for which the anisotropic effects can be easily ignored. A smooth piece of plastic doesn't exhibit much anisotropy as we spin it.

Surfaces such as brushed steel have elongated rather than round highlights even when the light source being reflected is round, see Figure 3.5. Surfaces with elongated highlights in one direction are referred to as being anisotropic reflectors.



**Figure 3.5:** *Anisotropic materials have elongated specular highlights rather than round [13].*

Although anisotropy might be caused by many different surface and material attributes, the effect is most easily demonstrated by looking at a grooved surface, see Figure 3.6. If the light direction is parallel to the grooves, it reflects just as it would from a smooth surface. If the light is perpendicular to the grooves, some of the light in the troughs is reflected differently.

### 3.4 Lambertian Reflectance

Lambertian, or ideal diffuse, reflectance, is in a sense the opposite of specular reflection. Instead of all light being reflected in a single direction, it is reflected in all directions with the same radiance [89]. The exitant radiance observed from all directions is directly proportional to  $\cos \theta_i$  and not dependent on the view direction. The constant of proportionality in this relationship is called diffuse reflectance  $\rho_d$ , also called surface albedo, is generally dependent on wavelength.

In order to ensure energy conservation, physically-based rendering approaches typically need  $\rho_d \in [0, 1]$  and introduce a normalization factor of  $\frac{1}{\pi}$ . Thus, the BRDF is constant at a

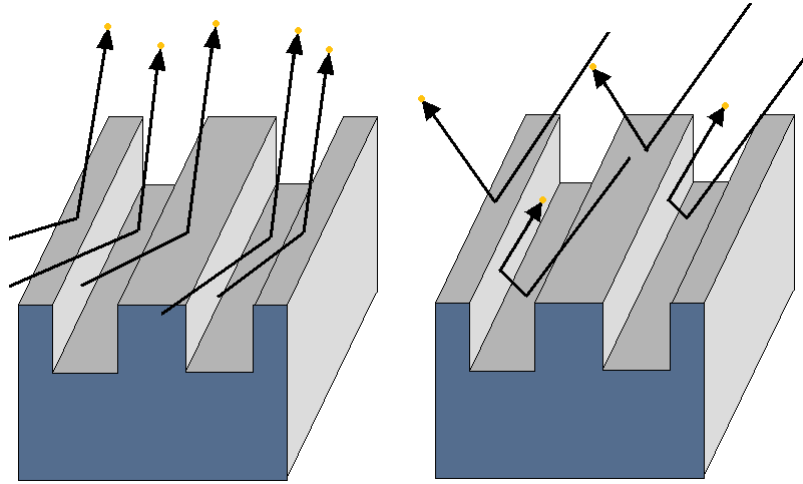


**Figure 3.6:** The grooves. Left: The light direction is parallel to the grooves. Right: The light direction is perpendicular to the grooves.

surface point  $\mathbf{x}$ :

$$f_r(\lambda, \mathbf{x}, \Theta_i \rightarrow \Theta_r) = \frac{\rho_d(\lambda, \mathbf{x})}{\pi}. \quad (3.17)$$

In real-time rendering  $\frac{\rho_d}{\pi}$  is usually simply substituted by a diffuse color  $C_d$ . If we substitute the absolute radiometric quantity radiance with some abstract *intensity*  $I$ , we get reflected intensity:

$$I_r = C_d I_i \cos \theta_i. \quad (3.18)$$

## 3.5 Phong Reflectance

The Phong model introduced in [59] was originally expressed as a reflectance function for setting shades in an image, rather than as a BRDF formulated for computing radiance. The goal of the model was not to accurately simulate light transfer, but to give the impression of a threedimensional shaded surface illuminated by a directional light source. The original model sets the color of the specular highlight to the color of the incident light, which creates the synthetic, plastic-like look. This is because a typical plastic has a transparent substrate with embedded color particles. So the light reflected specularly at the surface mostly retains its color, while the light that penetrates into the surface is likely to be reflected multiple times at the color particles, resulting in a mostly diffuse, colored reflection. The reflected intensity is given by the following formula:

$$I_r = (k_d C_d (\mathbf{N} \cdot \mathbf{L}) + k_s C_s (\mathbf{V} \cdot \mathbf{R})^e) I_i, \quad (3.19)$$

where  $C_s$  is specular color,  $\mathbf{N}$  is the surface normal,  $\mathbf{L}$  is a unit vector pointing in the direction of the light,  $\mathbf{V}$  is a unit direction vector pointing towards the view position and  $\mathbf{R}$  is in the direction of perfect specular reflection, see Figure 3.7. To ensure energy conservation, scaling coefficients  $k_d, k_s$  satisfy  $k_d + k_s \leq 1$ . The exponent  $e$  (called shininess coefficient) determines the sharpness of the gloss.

Note that the above formula is not exactly BRDF, it is a simplification of the rendering equation. This rendering equation, however, includes BRDF. In real-time rendering [12], terms  $C_s$  and  $I_i$  are simply replaced by the specular RGB color and the illuminant color, respectively.

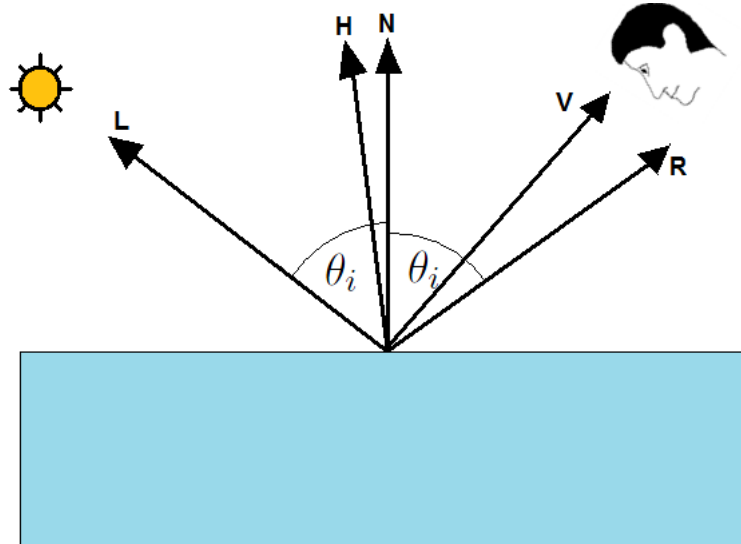


**Figure 3.7:** *The geometry of reflection.*

Soon after the Phong model was first published, Blinn introduced an alternative form. Blinn noted that mirror reflections are only observed when the surface normal is aligned with the halfway vector  $\mathbf{H}$ , which is the bisector of the angle between the vector to the source  $\mathbf{L}$  and the vector to the viewer  $\mathbf{V}$ , see Figure 3.7. Many systems use version of Phong reflectance where  $(\mathbf{V} \cdot \mathbf{R})$  is replaced by  $(\mathbf{N} \cdot \mathbf{H})$ , and it is often referred to as the Blinn-Phong model.

### 3.6 Ward Reflectance

In [87] Ward proposed an empirical anisotropic shading model. It is similar to the Phong model, except that rather than using the cosine term to a power, it uses an exponential function. The exponential term is parameterized by an average slope of the microscopic surface roughness.

The Ward model in the terms of BRDF is:

$$f_r(\Theta_i \rightarrow \Theta_r) = \frac{\rho_d}{\pi} + \rho_s \frac{1}{\sqrt{\cos \theta_i \cos \theta_r}} \frac{e^{-\frac{\tan^2 \theta_h}{\sigma^2}}}{4\pi\sigma^2}, \quad (3.20)$$

where  $\theta_r$  is the angle between  $\mathbf{N}$  and  $\mathbf{V}$ ,  $\theta_h$  is the angle between  $\mathbf{N}$  and  $\mathbf{H}$  (see Figure 3.7). The parameters  $\rho_d$  and  $\rho_s$  are spectral reflectance factors, that control the color of the diffuse and specular reflection. The value of  $\sigma$  represents the standard deviation of the microfacet slope, that models surface roughness by determining the spread of the specular lobe (see Figure 3.8). Small values of  $\sigma$  (i.e., less than 0.1) model a very nearly smooth surface. Normally,  $\sigma$  is adjusted by the user to get a particular appearance, or by fitting measured BRDF data, rather than somehow trying to measure the shape of the microscopic surface.

The Ward's model can be expressed in both isotropic and anisotropic forms. The isotropic Ward model in the form for real-time rendering is given by:

$$I_r = (k_d C_d + k_s C_s \frac{e^{\frac{(\mathbf{N} \cdot \mathbf{H})^2 - 1}{(\mathbf{N} \cdot \mathbf{H})\sigma^2}}}{4\pi\sigma^2 \sqrt{(\mathbf{N} \cdot \mathbf{L})(\mathbf{N} \cdot \mathbf{V})}}) I_i (\mathbf{N} \cdot \mathbf{L}). \quad (3.21)$$

The specular highlight is controlled by a roughness factor  $\sigma$  that is constant across the surface.

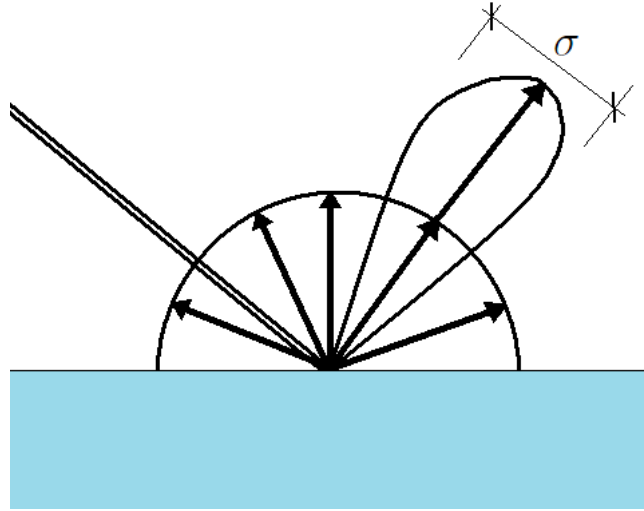


**Figure 3.8:** *The light scattering at the rough surface. The length of the arrows corresponds proportionally to the intensity redirected to particular direction.*

In the anisotropic case, the roughness factor is defined in two orthogonal directions on the surface. This creates an anisotropic effect in the specular highlight as the view direction changes. The anisotropic Ward model is given by:

$$I_r = (k_d C_d + k_s C_s \frac{e^{-2 \frac{(\mathbf{T} \cdot \mathbf{H})^2 + (\mathbf{B} \cdot \mathbf{H})^2}{\sigma_T^2 + \sigma_B^2}}}{1 + (\mathbf{N} \cdot \mathbf{H})}) I_i (\mathbf{N} \cdot \mathbf{L}), \quad (3.22)$$

where  $\mathbf{T}$  is a unit vector in the plane of the surface that is perpendicular to  $\mathbf{N}$  (i.e., the tangent) and  $\mathbf{B}$  is a unit vector in the plane of the surface that is perpendicular to both  $\mathbf{N}$  and  $\mathbf{T}$  (i.e., the binormal).

Anisotropic reflection has a significant impact on appearance, but for a complicated object its effect is only clear when the effect of isotropic or anisotropic reflection with a different orientation is displayed.

## 3.7 Cook-Torrance Reflectance

The Cook-Torrance model is a physically-based microfacet model that is focussed on (glossy) specular reflection [9]. It uses the surface roughness model developed by Torrance & Sparrow in [83]. This model treats surface as a collection of microscopic facets. The macroscopic optical properties of a surface are then analytically derived from properties of individual facets and statistical distributions of such properties.

### 3.7.1 Microfacet Distribution

Although, the surface has a normal  $\mathbf{N}$ , at a microscopic level the surface has height variations that result in many different surface orientations at a detailed level. At the perfectly flat surface a viewer is able to see light source, if  $\mathbf{H}$  is in the direction of surface normal  $\mathbf{N}$ . However, due to different surface orientations at a detailed level (see Figure 3.9), light source may be partially seen at surface positions where  $\mathbf{H}$  is not at direction of the surface normal. At this particular positions, however, surface normal  $\mathbf{N}$  has the same direction as a microfacet normal  $\mathbf{A}$ .

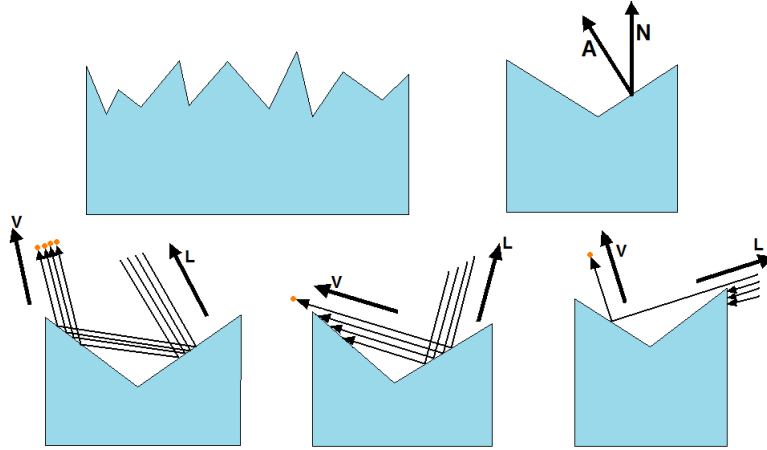


**Figure 3.9:** *Microfacet geometry. Upper left: Surface composed of microfacets. Upper right: Single V-cavity with normal  $\mathbf{A}$ . Bottom row: Interaction between microfacets, from left to right: interreflection, masking, shadowing.*

Rather than explicitly model the small geometric features, general reflectance functions use statistical models. Statistical models are used because the variation in surface height is assumed to be irregular and random.

A statistical model for surfaces in reflectance models generally takes the form of giving the distribution of facets that have a particular slope. One possibility is the Gaussian distribution of surface slopes considered by Blinn in [5]:

$$D = ce^{-\frac{\alpha^2}{m^2}}, \quad (3.23)$$

where  $c$  is an arbitrary constant,  $\alpha$  is the angle between surface and facet normal, and  $m$  is the root mean square slope of microfacets parameterizing the surface's roughness.

Most commonly used, however, is the Beckmann distribution function. It is based on physical theory on scattering of electromagnetic waves and does not require the introduction of arbitrary constants. The formula is:

$$D = \frac{e^{-\frac{\tan^2 \alpha}{m^2}}}{m^2 \cos^4 \alpha}. \quad (3.24)$$

If we assume V-grooved surface (Figure 3.9), then we need to count with self shadowing and masking. The geometric attenuation factor  $G$  models the geometric effects shadowing and masking between microfacets that occur at larger angles of incidence or reflection. It is defined by the formula:

$$G = \min\left(1, \frac{2(\mathbf{H} \cdot \mathbf{N})(\mathbf{V} \cdot \mathbf{N})}{\mathbf{H} \cdot \mathbf{V}}, \frac{2(\mathbf{H} \cdot \mathbf{N})(\mathbf{L} \cdot \mathbf{N})}{\mathbf{H} \cdot \mathbf{V}}\right). \quad (3.25)$$

### 3.7.2 Cook-Torrance Model

The Cook-Torrance model provides a good reproduction of the appearance of many real materials. Especially metallic surfaces profit from the increased realism of the specular factor. Effects like the characteristic color shift towards the color of the incident light near grazing angles and the off-specular peak for very rough surfaces greatly improve the perceived realism of renderings. The off-specular peaks are the consequence of shadowing and masking causing asymmetries.

Specular component of this model can be compactly written as:

$$\frac{F_r DG}{\pi(\mathbf{N} \cdot \mathbf{L})(\mathbf{N} \cdot \mathbf{V})}, \quad (3.26)$$

where  $F_r$  is Fresnel term given by the formula 3.13, where incident angle  $\theta_i$  is angle between  $\mathbf{L}$  and  $\mathbf{H}$  (we assume mirrorlike microfacets which are reflecting the light from a source to the viewers direction).

Advantage of this model is its modular structure that allows to easily replace components with more accurate or more efficient versions. Disadvantages are the high computational costs and the unintuitive parameters, that are hard to tweak if no measured data is available.

### 3.8 Psychophysically-Based Light Reflection Model

In paper [62] Ďurikovič and Ershov have proposed method to find a paint composition correspondent to a given BRDF. In this method paint composition is derived from psychophysical attributes such as gloss, shade and glitter.

In paper [37] is introduced a reparametrization of an isotropic version of Wards reflectance model. This reparametrization results in a psychophysically-based light reflection model, where the dimensions of the model are intuitive and perceptually meaningful, and variations along the dimensions are perceptually uniform.

This model is based on two dimensional perceptually uniform gloss space. Two perceptually meaningful axes in this space have been assigned. First, the contrast gloss  $c$ , second, the distinctness-of-image (DOI) gloss  $d$ . Contrast gloss is perceived relative brightness of specularly and diffusely reflecting areas, while DOI gloss is perceived sharpness of images reflected in a surface (see Figure 3.10).

The expressions of the physical parameters of the equation 3.20 in terms of the perceptual ones are following:

$$\rho_d = f^{-1}(L^*) \quad (3.27)$$

$$\rho_s = (c + \sqrt[3]{f^{-1}(L^*)/2})^3 - f^{-1}(L^*)/2 \quad (3.28)$$

$$\sigma = 1 - d \quad (3.29)$$

where  $L^*$  is CIE LAB lightness of diffuse reflectance and  $f$  is the CIE LAB lightness function normalized in  $[0,1]$ .

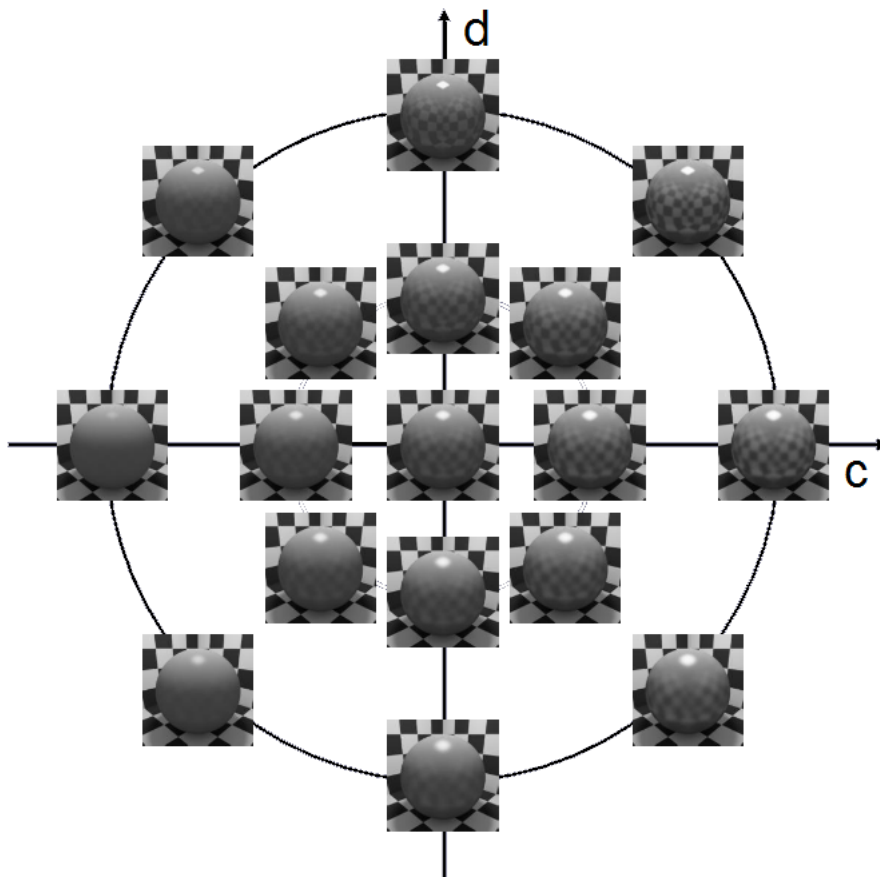


**Figure 3.10:** *The contrast gloss  $c$  and DOI gloss  $d$  in twodimensional space [56].*

## Chapter 4

# Measurement

Measuring how materials scatter light was a topic of interest long before computer graphics realistic image synthesis evolved. Broadly speaking, two classes of measurement systems had developed: high accuracy BRDF measurement devices and industrial spot measurement devices. In particular, high accuracy systems give an idea of the magnitude of uncertainty that can be expected from even carefully constructed systems. Industrial spot measurement systems give an idea of how powerful relatively simple measurements can be.

### 4.1 BRDF Measurement

Typical measurement systems consist of a light source, positioning system to hold a sample of the target material to be measured, and a sensor that records the quantity of light scattered from the target. Since extraneous light reflecting from the target to other surfaces in the setup is a source of error, a room with everything coated in black is used for measurements. Since accurate positioning is needed, the system is generally mounted on a heavy optical table to prevent vibrations from movements in the room affecting the positions of the source, target, and sensor.

The definition of BRDF, is in terms of infinitesimal incident and reflected solid angles, and an infinitesimal area on the target surface. Since the components of any system will be finite in size, some uncertainty is inherent in the process. The incident and reflected angles and target illuminated area can be made very small, but this results in very low quantities of energy being scattered that are difficult to measure accurately.

To obtain the absolute value of the BRDF, the detected light from a sample has to be compared to the incident. A typical way of doing this is to compare the detected light to that from a known sample.

Typical gonioreflectometer consists of mechanical elements to ensure the four degrees of freedom required to measure the complete reflectance function [1]. To acquire BRDF data this devices require to move the receptor aperture and the light source. Disadvantages of these devices are their time inefficiency and inaccuracy related to their mechanism.

To decrease degrees of freedom the spherical sample rather than a planar sample can be used [47, 39]. This allows us to keep the camera (receptor aperture) in fixed position. Photography of the example of such a system is depicted in Figure 4.1.

In paper [68] is introduced BRDF measurement system without any mechanical element. This system consists of multiple cameras mounted on a hemispherical gantry. Each camera is equipped with a flash unit, see Figure 4.2.

Minimalistic concept of above approach led to an LED-only BRDF measurement device, see Figure 4.3. The device consists of an aluminum hemisphere with many embedded LEDs,



**Figure 4.1:** *Left: A photograph of BRDF measurement system. Right: The measurement target, a sphere painted with car paint [30].*

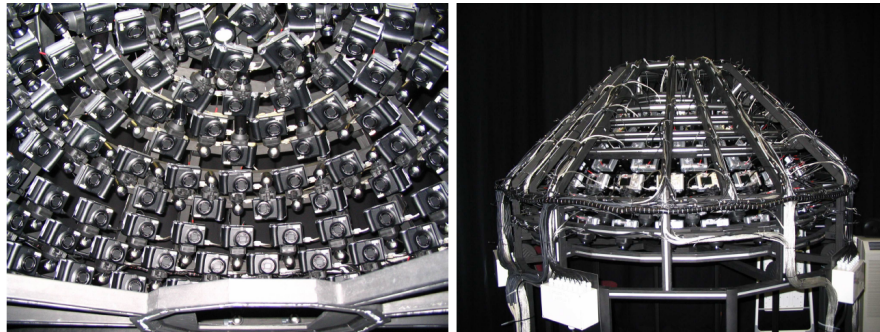


**Figure 4.2:** *The BRDF measurement device consists of 151 digital consumer cameras mounted on a hemispherical gantry [68].*

all pointing toward the center of the hemisphere. These LEDs are used either as the light source and the photoreceptor. A lens is used with each LED to improve the optical performance. During operation, each LED is turned on momentarily. While one LED emits light, all others measure the reflected light from the sample. Next, a different LED is chosen to emit light, and the remaining ones (including the previous emitter) measure the reflected light.

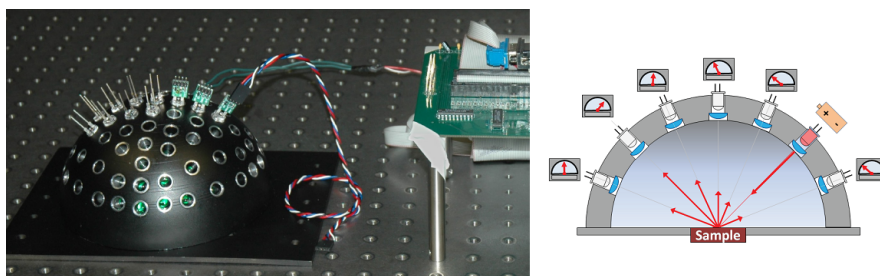


**Figure 4.3:** *An LED-only BRDF measurement device [4].*

## 4.2 Industrial Measurement

Industrial applications require the efficient assessment of surface appearance. Product manufacturers need to test whether the products they are producing (paint, plastic covering, paper, etc.) meet design criteria. Because of the time and expense of a full BRDF measurement, devices have been developed that characterize surface appearance with a small number of

measurements. Unlike high accuracy BRDF measurement devices, these devices are available on the market, see Figure 4.4. Broadly speaking, two classes of devices are common: one for color assessment and another for haze or gloss.



**Figure 4.4:** Left: Multi Gloss 268 [26]. Right: Minolta BC-10 Colorimeter [13].

Common color instruments are colorimeters that return color values reflected by materials under standard illuminants in standard color spaces (i.e. CIE LAB). To measure the diffuse color and the albedo, the illuminant is a hemisphere over the sample patch. Receptor aperture is positioned above the surface and directed to measure reflected light under  $8^\circ$  from direction of the surface normal.

Industrial devices designed to measure qualities such as gloss and haze are called glossmeters. The measurement of the specular gloss consists of comparing the luminous reflectance from tested specimen to that from a gloss standard, under some geometric and spectral conditions well defined by national or international standards e.g. ISO 2813 [22, 19].

Those standards usually prescribe the measurement to be taken at angles  $20^\circ$ ,  $60^\circ$  and  $85^\circ$  to the surface normal, because these degrees of specular gloss measurements offer numerical values which are roughly linearly correlated over a range of values to perceived gloss of high-gloss, medium-gloss and low-gloss surfaces, respectively. The numerical gloss values ranges from 0 to 100.

#### 4.2.1 Virtual Glossmeter

Measurement of light reflection from the surface of the material was of the concern even before the computer graphics started to deal with photorealistic rendering. Gloss measurement is already in the 30's of the twentieth century dealt by Hunter, who categorized gloss into several groups [35] and helped design the first standards.

American Society for Testing and Materials (ASTM) then established standard measurements of gloss and haze. An overview of these appearance measurement standards is offered in the paper [88], where these standards and simple appearance measurements were applied to realistic image synthesis. Given existing computer graphic reflection models such as the Phong model, the Ward model and the Cook-Torrance model, a correspondence were indicated between the parameters of these models and appearance measurement scales such as gloss and haze. This provides an appearance based rational and a simple measurement scheme for setting the parameters of these models. Main contribution of the paper [88] is an introduction of the algorithm to the virtual measurement of gloss from BRDF, fulfilling ASTM standards.

Devised algorithm of the virtual glossmeter computes gloss value of the virtual surface using assigned BRDF under specific angle. Gloss values are directly dependent upon the measured flux reflected off the surface and passing through the receptor aperture. The integration of this flux begins by subdividing the source aperture. For each sample point on

the source, the receptor aperture is subdivided. Figure 4.5 shows an example of the flux due to one subdivided source element (cell) passing through the receptor. After this flux is determined, the next source cell is chosen and the process is repeated.

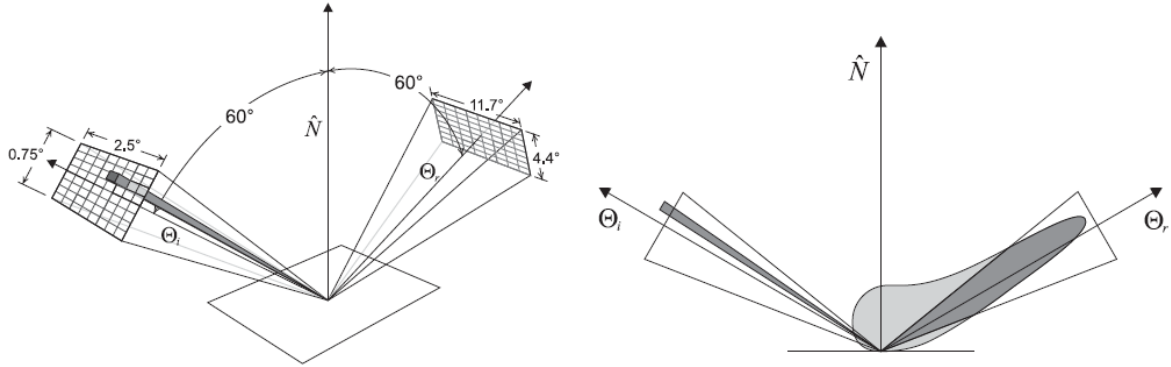


**Figure 4.5:** Left: Subdivision of glossmeter apertures using the 60 degree specular gloss. The source and receptor apertures are oriented in directions  $\Theta_i$  and  $\Theta_r$ , 60 degrees down from the surface normal,  $\hat{N}$ , in the plane of incidence. Right: Flux passing through receptor aperture due to one source aperture subdivision. Aperture sizes are not to scale [88].

The gloss value  $G$  is computed by the following formula:

$$G = 100 \frac{\sum_{k=1}^K \sum_{j=1}^J \rho(\hat{s}_j, \hat{d}_k) d\Omega_{S_j} d\Omega_{D_k}}{\sum_{k=1}^K \sum_{j=1}^J F(n, \hat{s}_j) \delta(\text{mirror}(\hat{s}_j) - \hat{d}_k) d\Omega_{S_j}}, \quad (4.1)$$

where  $d\Omega_{S_j} = \hat{s}_j \cdot \hat{N} d\omega_{S_j}$ ,  $d\Omega_{D_k} = \hat{d}_k \cdot \hat{N} d\omega_{D_k}$ ,  $F$  is the Fresnel reflectivity for unpolarized light,  $n$  is the refractive index of the standard, and  $\text{mirror}(\hat{s}_j)$  is the unit mirror direction vector of  $\hat{s}_j$ . Solid angles  $d\omega_{S_j}$  and  $d\omega_{D_k}$  are subtended by  $j^{\text{th}}$  cell of the source at certain point of the sample and  $k^{\text{th}}$  cell of receptor aperture, respectively.  $\hat{s}_j$  and  $\hat{d}_k$  are the unit direction vectors (from certain point of the sample) pointing toward  $S_j$  and  $D_k$ , respectively. The mirror direction vector can be computed with:

$$\text{mirror}(\hat{s}_j) = 2(\hat{s}_j \cdot \hat{N})\hat{N} - \hat{s}_j. \quad (4.2)$$

The delta function is:

$$\delta(\bar{v}) = \begin{cases} 1 & \text{if } |\bar{v}| < \epsilon \\ 0 & \text{if } |\bar{v}| \geq \epsilon \end{cases}. \quad (4.3)$$

## Chapter 5

# Project of Dissertation

In this chapter we define and discuss our major goals and research interests. We also define some problems in material modeling and try to suggest solutions to these problems.

### 5.1 Research Interests and Goals

Material appearance of the scene objects is the basis of the image synthesis in computer graphics. Besides the image synthesis, there are lots of another interesting applications of the material appearance modeling. For example in the paint and coatings industries, designers are required analyze many design variations in a short time and at low costs [24, 18]. To help them a computer graphics program can be used that allows the user to interactively adjust the surface reflection properties of a paint and visualize the appearance of that paint on a three dimensional surface [48].

Another utilization of the digital appearance modeling of materials is in the field of the digital preservation of the cultural heritage. For example in [21] is introduced a method for rendering of the Japanese lacquer ware, a prominent Far East Asian handicraft art.

The major goal of our research is measurement and acquirement of the data that represent the optical properties of real materials, analysis of these data and the proposal of the method to render plausible appearance of the real materials. Problem of the data acquirement is outlined in chapter 4. In order to analyze the material appearance it is reasonable to decompose independent optical properties (e.g. diffuse and mirror reflection are independent according to the models from chapter 3) and treat each separately. The evaluation of the material appearance may be accomplished by observation or physical analysis of the examined material.

Rendering a digital image requires computing individual pixel colors, representing the appearance of an object as seen from the viewer. The finite resolution of the image, as well as the great variability of object colors even for neighboring locations, make it impossible to define a pixel color as simply the color of the visible object at that pixel. The essential operation of the rendering is to determine how a given point in space will appear from the view point: either this determination is carried out for all elements of a scene, or it is only performed for elements that are visible in the image [11].

Major areas of our ongoing research are:

- Editing of the material appearance of the objects depicted in 2D images
- Transport of the material appearance between objects depicted in 2D images
- Implementation of the virtual goniospectrophotometer
- Measurement of gloss and albedo of real materials and creation of the sufficient BRDF based on these data
- Analysis of the metallic flakes and rendering of the sparkling effects
- Industry based modeling and rendering of the spectral effects

## 5.2 Solutions and Techniques

In the following sections we overview main problems and suggest possible solutions to the goals of our research.

### 5.2.1 Appearance editing

To allow user to edit such complex datasets of the measured spatially varying BRDF (SVBRDF) is not acceptable. SVBRDF is BRDF measured at multiple surface coordinates of the sample. To make editing easier a framework was introduced in paper [57]. In this system, a user specifies a small number of editing constraints with a 3D painting interface which are smoothly propagated to the entire dataset through an optimization that enforces similar edits are applied to areas with similar appearance.

In [44] is the "inverse shade tree" (see Figure 5.1) created from measured data. The leaves of these tree are sampled 1D and 2D functions that capture both the directional behavior of individual materials and their spatial mixing patterns. To edit the material appearance users change these functions. A rendering shading tree representing multiple BRDFs with possibility to combine them was devised by Āurikoviĉ and Kolchin [Durikovic02renderingof]. This approach was later extended to enable the user interactive editing of BRDF stored in shading tree.

A technique that can be useful in editing and transforming material appearance of the object depicted in single image is called appearance manifolds. Appearance manifold is a manifold which points are attributed to the particular appearance property. This technique was used for example in editing material appearance attributed to weathering of the object depicted in single 2D image [75, 86].

### 5.2.2 Material appearance transfer from the object depicted in a image to another object

To our knowledge no attempt of appearance transfer between images have been made so far. However, several works are devoted to the estimation of the optical parameters from the observation of how the material surface reflects light [81, 70, 92, 67]. Methods based on image analysis may require multiple images [70, 92] or scene geometry [7, 6].

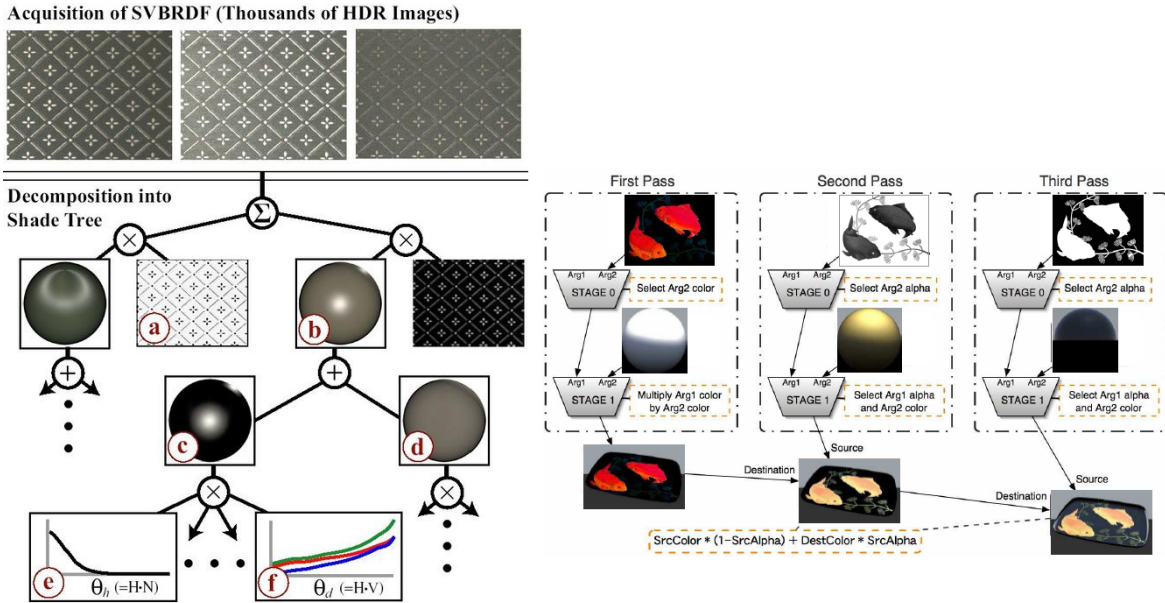


**Figure 5.1:** Left: Decomposition of the appearance and optical properties of an anisotropic material into the shade tree [44]. Right: Decomposition of a material into BRDF components [18].

Work [16] devoted to classification of reflectance properties of surfaces based on the predictable statistical structure of real-world illumination requires single monochrome images. Method in [65] estimates the surface radiance function from single images. This method is based on the Gauss map between the surface and a unit sphere and is applicable only when the light source and viewer directions are approximately equal.

To analysis of the optical properties of the materials such as plastics a reflection model so-called "dichromatic model" can be use [41]. This model assumes that the color of the light source is different from that of the surface material. The resulting color of light reflected from the surface of the material is then a weighted sum of material color and light color. By color histogram analysis of illuminated object can be the diffuse color and its surface roughness which affects the perception of gloss estimated [81, 53].

In analysis of the reflected light is useful to distinguish diffuse and mirror component [3]. In the field of computer vision there are several methods to separate the mirror component from the resultant intensity of reflected light. Some use a polarizing filter, other multiple images [46], but there are also methods [73, 71, 78, 38] which operate just on a single image under assumption that the lighting model is dichromatic. One of the first methods using dichromatic model was based on an analysis of the distribution of colors in RGB space, which results in two clusters. These clusters represents a specular component and a diffuse component of the reflected light [73, 42]. In [71] is introduced fast and robust method to separate specular component of color image, which is based on two-dimensional representations of color, where diffuse color is represented by the color with maximum tone. Method that uses a projection of the image colors toward the point with the lowest observed intensity is described in [78]. This projection is in RGB space along the direction of the color vector of the illumination color.

Given that the reflection of light from the object depends on the orientation of the surface normals, the knowledge of the surface normals can help in analyzing the reflectance. There are several algorithms [15, 54, 93, 60, 43] to estimate the shape from a single image (shape from shading), although in general there is no clear solution to this problem. First, the problem was

formulated as a problem of finding the solution of a nonlinear first-order partial differential equation called the brightness equation [32]. Later it was shown that from a single image one can find estimation of the orientation of normals up to an orthogonal transformation.

In [51] we have proposed a method to transport the appearance from one object depicted in single image to another object depicted in another image. In this approach both images are decomposed to their specular and diffuse component. Diffuse component of both images serves as input data to a shape from shading algorithm to recover surface normals of the objects. Subsequently each pixel's specular and diffuse component of the second image is changed according to recovered normals and pixels of the first image. See chapter 6 for more details.

Accuracy of the appearance transport rely on the shape from shading algorithm. Inaccuracy of surface normal recovery causes noise in diffuse component and displacement of the specular highlight. First problem can be solved by the linear regression since intensity of the diffuse component is linear function of  $(\mathbf{N} \cdot \mathbf{L})$ , see equation 3.18. Second problem is more complex. It may be solved by determination of the intensity function of  $(\mathbf{N} \cdot \mathbf{H})$  from highlight peak (in highlight peak  $\mathbf{H} = \mathbf{N}$ ) through specular highlight in  $\mathbf{L}$ - $\mathbf{V}$  plane.

### 5.2.3 Virtual goniospectrophotometer

One of our goals is to design and implement a computer program devoted to the measurement of gloss and SPD of the reflected light from samples represented by BRDF. In practice, these measurements are performed by devices from chapter 4 using real material samples. Aim of the program is to perform these measurements on virtual samples represented by BRDF. These measurements can be compared with actual measurements on real samples and then precision of computer representation can be evaluated [76].

Goniospectrophotometer should consist of a standard light source and receptor (luminous flux sensor). Sample of the material input could be represented by a BRDF (in case of nonhomogeneous surface by SVBRDF). Users should be able to change the area and location (with respect to the sample surface) of the light source and the receptor. These settings allow of measurement with different standards.

Calculation of the luminous flux can be performed by splitting of the light source and receptor aperture. Then, for each cell can be calculated luminous flux, which is reflected from the sample and then passes through the receptor cell, see Figure 4.5.

The real measuring devices such as glossmeters can not measure the light reflection at a single point of the sample, but measure reflection in a small region. For nonhomogeneous surfaces such as metallic or pearlescent varnishes has a sample different BRDF in each point. It is therefore necessary to divide the sample into smaller parts and make a calculation in each of its part. Functionality of the program should be extended to implementation of the virtual colorimeter.

### 5.2.4 Measurement of gloss and albedo

One utilization of the program mentioned above is measurement of the albedo and the gloss at angles  $20^\circ$ ,  $60^\circ$  and  $85^\circ$  to the surface normal performed on analytical BRDF such as Cook-Torrance or Ward model. These three measurements of gloss do not provide enough data to construct whole BRDF of the measured material. However, in general some attributes of BRDF may be dependent on gloss values. For example measurements in [10] suggests that there is certain dependence between DOI and gloss under  $85^\circ$ . Therefore we suppose that majority of the materials is able to approximate by some analytical BRDF with parameters attributed to gloss values.

If this analytical BRDF based on the standard measurements exists, then this BRDF may

be acquired by the reparametrization of known analytical model. Multiple measurements of the gloss may be performed by virtual goniospectrophotometer with different parameters of BRDF of the known model. These measurements may be performed for example in space from Figure 3.10. Thus rough approximation of the material's BRDF may be acquired just by measurements using commercial devices such as the glossmeter and colorimeter (see Figure 4.4). This should be possible because reflected light measured by the glossmeter under grazing angles is more dependent to BRDF attributes like DOI, while light reflection under steeper angles is more related to the diffuse reflectance.

### 5.2.5 Sparkling analysis and rendering

Paint coatings containing metallic flakes exhibit sparkling and depth effects [17, 85]. The light scattering within the system of metal flakes or particles creates the sparkling and glare effects with radial streaks of light around high intensity particles, see Figure 5.2.



**Figure 5.2:** *Sparkling effect* [25].

The ray reflected by a flake can reach observer either directly (in one scattering), or after several scatterings (by other flakes or by the substrate or by the paint-air boundary). However, each reflection substantially attenuates light, thus it is the flakes seen "directly" that are the brightest; it is them that look like sparkles [72].

Sparkles can be represented by the texture. The idea of simulation of the sparkling is to calculate statistical characteristics of fluctuations due to scattering by flakes and then reproduce the paint texture by superimposing random fluctuations on the image obtained by standard rendering.

### 5.2.6 Rendering of the spectral effects

Chromatic dispersion causes the spatial separation of a white light into components of different wavelengths [52]. Spectral variation of the index of refraction is what causes different wavelengths of light to bend a different amount when they pass through glass, and causes white light to split into a rainbow of colors in a prism, see Figure 2.1.

Dispersion is rendered by following separate ray paths for different wavelengths, rather than following one geometric path for R, G, and B [20, 29].

Intense color can appear when light passes through a thin film, such as an oil slick on water on the street after it rains. In this instance, thin is defined as a length on the order of the wavelength of light. Thin film interference (see Figure 5.3) occurs when the thickness of the film is on the order of a wavelength of light. The phase of a wave, that is, where it has peaks and valleys, switches when light reflects off a boundary from lower to greater index of refraction, but does not change when reflecting from greater to lower index of refraction.

Rendering of the spectral effects require spectral data (e.g. sampled SPD function). Since

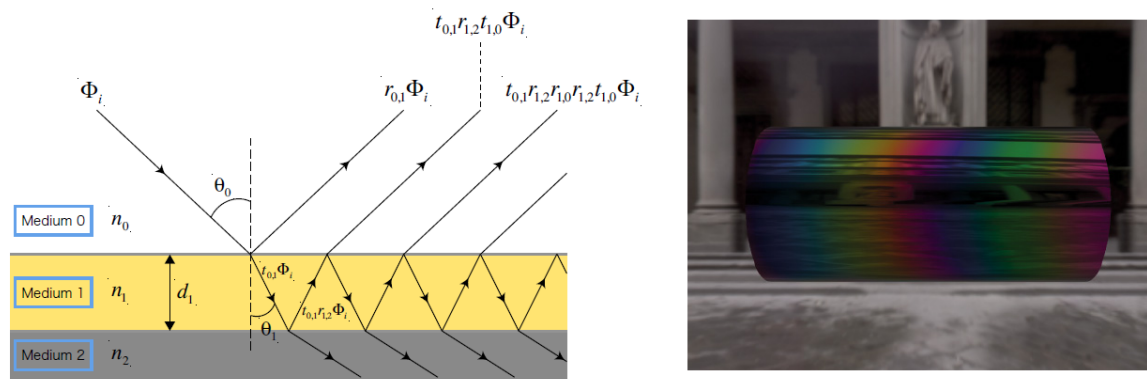


**Figure 5.3:** Left: Multiple reflection on single layer surface, where  $r$  denotes path of reflected ray,  $t$  denotes refracted path. Right: Chrome oxide thin film interference with increasing thickness from 100 nm to 400 nm [20].

graphics hardware utilizes just RGB color space, then rendering of the spectral effects on GPU is not straightforward, and requires more sophisticated approach.

# Chapter 6

## Preliminary Results

In this chapter we present results of our research focused to the material appearance transfer between two objects depicted in single 2D images. Our work has been introduced in [50]. In the following section we describe key ideas of our method and overview some of the results we achieved.

### 6.1 Material appearance transfer between images

Presented method is devoted to the appearance transformation of an object depicted in a single image. The goal is to achieve appearance of material depicted in another image called material image. Although, for the sake of simplicity we assume that depicted objects are lit by the white light source, the method [80] to estimation of the color of the illuminant could be used in general case.

#### 6.1.1 Separation of the Specular Component

In the process of the reflection analysis it is reasonable to separate the specular and diffuse reflection [63]. Inspired by papers [79] and [77] we devised simple solution to the problem of specular–diffuse separation.

Let us consider the dichromatic reflection model, where the color of highlight is a linear combination of specular and diffuse color. This model proves adequate for most materials such as inhomogeneous dielectrics. Under assumption, that the scene is lit by the white source and the diffuse color of the object is not desaturated, the diffuse component can be obtained by the projection along the illumination direction. Color of pixels in the specular highlight region of the image creates an highlight cluster in RGB color space, see Figure 6.1.

Maximum chromaticity is defined by the following formula:

$$\sigma(\mathbf{x}) = \frac{\max(I_r(\mathbf{x}), I_g(\mathbf{x}), I_b(\mathbf{x}))}{I_r(\mathbf{x}) + I_g(\mathbf{x}) + I_b(\mathbf{x})}, \quad (6.1)$$

where  $I_r(\mathbf{x})$ ,  $I_g(\mathbf{x})$  and  $I_b(\mathbf{x})$  are R, G and B components of the pixel at the image coordinates  $\mathbf{x}$ . Let  $\mathbf{d}$  is a vector in the RGB space defined as  $(I_r(\mathbf{x}), I_g(\mathbf{x}), I_b(\mathbf{x}))$ , where  $\mathbf{x}$  are coordinates of the pixel of the object in the image with  $\sigma(\mathbf{x}) = \max\{\sigma(\mathbf{y})|\mathbf{y} \in \Omega\}$ .  $\Omega$  is a region in the image where the object is in. At coordinates  $\mathbf{x}$  lies its most desaturated pixel. Let  $\mathbf{s}$  is a vector in the RGB space defined as  $(1, 1, 1)$  representing the direction of the illumination color. Diffuse component  $\mathbf{c}(\mathbf{x})$  of the pixel at  $\mathbf{x}$  with color  $\mathbf{p}(\mathbf{x})$  in the highlight cluster is then computed as the intersection of the line in the direction  $\mathbf{s}$  passing through  $\mathbf{p}(\mathbf{x})$  with the line in the direction  $\mathbf{d}$  passing through point  $(0, 0, 0)$ . In other words, the diffuse component

of the pixel at the coordinates  $\mathbf{x}$  with the color  $\mathbf{p}(\mathbf{x})$  is given by the following formula:

$$\mathbf{c}(\mathbf{x}) = \mathbf{p}(\mathbf{x}) + \mathbf{s} \frac{(-\mathbf{p}(\mathbf{x}) \times \mathbf{d}) \cdot (\mathbf{s} \times \mathbf{d})}{|\mathbf{s} \times \mathbf{d}|^2}. \quad (6.2)$$

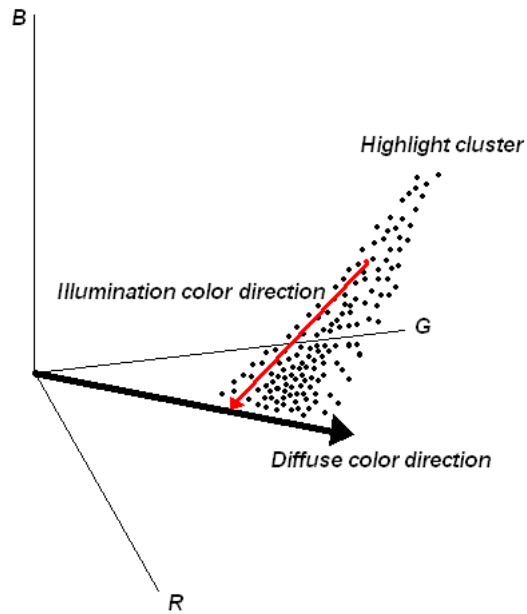


**Figure 6.1:** Color histogram in the RGB space.

Specular component can be derived by  $\mathbf{p}(\mathbf{x}) - \mathbf{c}(\mathbf{x})$ . Figure 6.2 shows an image of the sphere on top and two images obtained by decomposition into the diffuse and specular components.

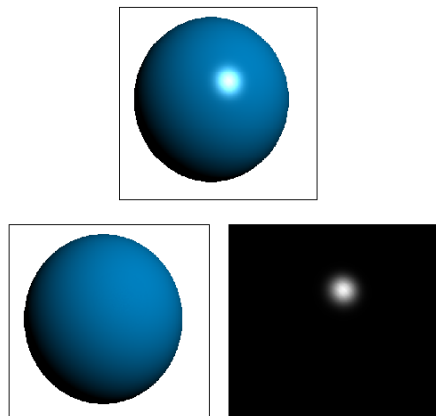


**Figure 6.2:** Original image and its diffuse and specular component image.

As clamping in the color space produces saturation of the color, it is reasonable to use one of the HDR color formats such as RGBE.

### 6.1.2 Shape from Shading

To calculate the normal vector  $\mathbf{N}(\mathbf{x})$  at surface point from an image of a surface a shape from shading algorithm can be utilized [90].

Let  $\mathbf{I}(\mathbf{x})$  is a greyscale image of the diffuse component, then according to Lambertian reflection it can be written as

$$\mathbf{I}(\mathbf{x}) = \eta(\mathbf{N}(\mathbf{x}) \cdot \mathbf{L}), \quad (6.3)$$

where  $\mathbf{L}$  is the illumination direction and  $\eta$  is the composite albedo. Obtaining of the 3D shape from a single shaded image is ill-proposed problem [61], therefore most of the algorithms incorporates regularization. The common assumption about surface shape is that the surface is locally spherical. The recovered shape can be expressed as depth  $Z(\mathbf{x})$  or surface normals, where  $Z$  directs toward the camera. An iterative method based on the discrete approximation of the surface gradients is proposed in [84].

Horn and Brooks have proposed to use the unit normal rather than the gradient [8]. This method is based on the minimization of  $\int_{\Omega} (\mathbf{I}(\mathbf{x}) - \mathbf{N}(\mathbf{x}) \cdot \mathbf{L})^2 d\mathbf{x}$ , where  $\Omega$  is a region in  $xy$ -plane.

Some shape from shading algorithms require known illumination direction. In papers [94, 58] are discussed some methods to estimate the illumination direction or surface albedo. The azimuth of illuminat in paper [45] is estimated as

$$\tau = \arctan \frac{\mathbf{E}\{I_y\}}{\mathbf{E}\{I_x\}}, \quad (6.4)$$

where  $I_x$  and  $I_y$  are the first-order partial derivatives of image intensity with respect to the local spherical coordinates, and the expectations are taken over the whole region. Since it is not clear how to evaluate the derivatives of image intensity with respect to local spherical coordinates, in our implementation of this method, we computed  $I_x$  and  $I_y$  as the partial derivatives of image intensity with respect to image coordinates.

The slant angle  $\gamma$  of the illuminant is computed according [94] as root of the polynomial

$$0 = 05577 - \frac{\mathbf{E}\{I\}}{\sqrt{\mathbf{E}\{I^2\}}} + 0.6240\cos\gamma + 0.1882\cos^2\gamma - 0.6514\cos^3\gamma - \\ -0.5350\cos^4\gamma + 0.9282\cos^5\gamma + 0.3476\cos^6\gamma - 0.4984\cos^7\gamma, \quad (6.5)$$

where  $\mathbf{E}\{I\}$  and  $\mathbf{E}\{I^2\}$  are the ensemble averages of the image intensities and the square of the image intensities, respectively.

We adopted the iterative scheme for minimisation of a functional, where the surface normal is updated by taking a local average, and adjusting it either toward or away from the source. Although for the images of perfect sphere these methods work quite well, for relatively complex images results are not very encouraging.

### 6.1.3 Transport of the Appearance

Proposed method requires two input images, first one is the material image  $\mathbf{I}_1(\mathbf{x})$ , depicting the object with required material appearance. Second input image is the object image  $\mathbf{I}_2(\mathbf{x})$  it is the original image of object which some appearance we would like to change. The goal of this method is to change pixels of the object in original image  $\mathbf{I}_2(\mathbf{x})$  to achieve the material appearance of the object depicted in material image  $\mathbf{I}_1(\mathbf{x})$ .

The color vector  $\mathbf{p}(\mathbf{x})$  of the pixel of the object at the coordinates  $\mathbf{x}$  can be described as follows:

$$\mathbf{p}(\mathbf{x}) = (\mathbf{N}(\mathbf{x}) \cdot \mathbf{L})\mathbf{d} + w_i(\mathbf{x})\mathbf{s}, \quad (6.6)$$

where  $\mathbf{d}$  is the diffuse color vector,  $\mathbf{s} = (1, 1, 1)$  is the illumination color,  $\mathbf{H}$  is the bisector vector between the light and the viewing direction, and  $w_i(\mathbf{x})$  is the function of  $\mathbf{N}(\mathbf{x}) \cdot \mathbf{H}$ . First term represents the diffuse component of the pixel at the coordinates  $\mathbf{x}$ , and second term represents the specular component. Applying the decomposition described above to each of the input image produces a specular component image and a diffuse component image. To estimate the geometry of both objects depicted in input images a shape from shading method is used. Results of proposed steps are captured in Figure 6.3.

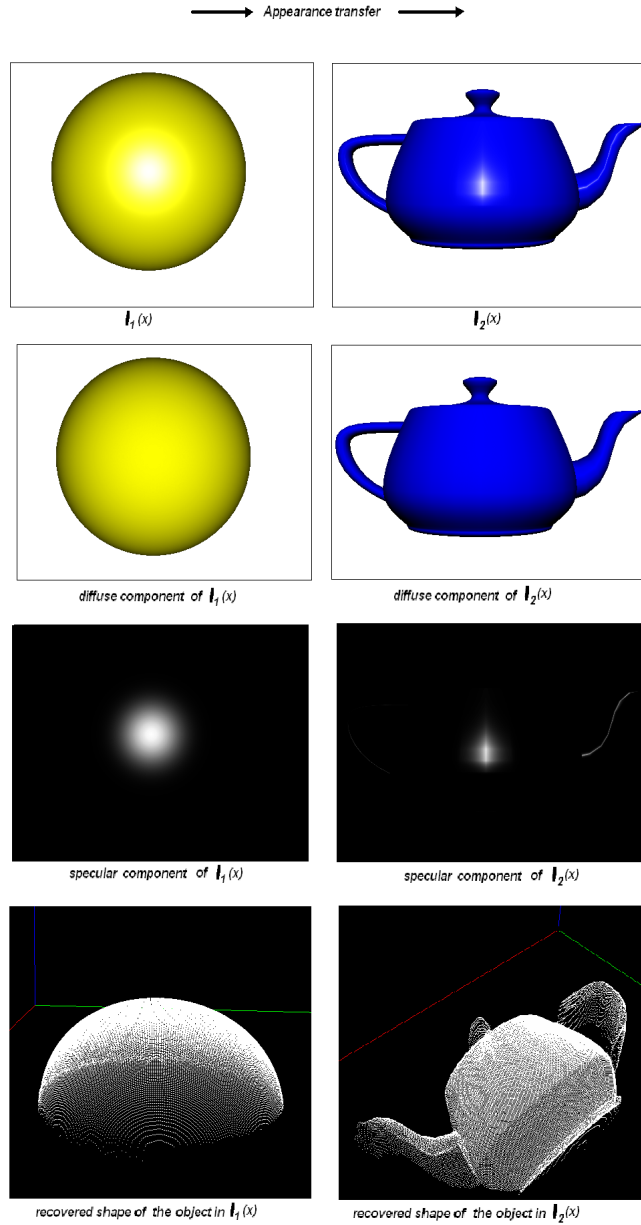


**Figure 6.3:** Steps required in the process of the transfer.

To estimate the surface normals, method described in [8] have been used. Let  $\mathbf{N}_1(\mathbf{x})$  is the normal map of the object in the material image  $\mathbf{I}_1(\mathbf{x})$  and  $\mathbf{N}_2(\mathbf{x})$  is the normal map of the object image  $\mathbf{I}_2(\mathbf{x})$ . If  $\mathbf{x}_1$  are coordinates of the most brightest pixel in the specular component image of the material image and  $\mathbf{x}_2$  in the specular component of the object image. Then the bisector vector  $\mathbf{H}_1$  can be approximated by  $\mathbf{N}_1(\mathbf{x}_1)$  and  $\mathbf{H}_2$  can be approximated by  $\mathbf{N}_2(\mathbf{x}_2)$ . Let  $\mathbf{L}_1$  represents illumination direction in the material image and  $\mathbf{L}_2$  in the object image.  $\mathbf{L}_1$  is obtained as the reflection  $\mathbf{L}_1 = 2(\mathbf{V} \cdot \mathbf{H}_1)\mathbf{H}_1 - \mathbf{V}$  and similarly  $\mathbf{L}_2 = 2(\mathbf{V} \cdot \mathbf{H}_2)\mathbf{H}_2 - \mathbf{V}$ ,

where  $\mathbf{V} = (0, 0, 1)$ .

Let  $\mathbf{A}$  and  $\mathbf{B}$  are tabular representations of a mapping from  $\mathbb{R}$  to RGB space

$$\mathbf{A} = \{(\mathbf{N}_1(\mathbf{x}) \cdot \mathbf{L}_1, d(\mathbf{I}_1(\mathbf{x}))) \mid \mathbf{x} \in \Omega_1\}, \quad (6.7)$$

$$\mathbf{B} = \{(\mathbf{N}_1(\mathbf{x}) \cdot \mathbf{H}_1, s(\mathbf{I}_1(\mathbf{x}))) \mid \mathbf{x} \in \Omega_1\}, \quad (6.8)$$

where  $d(\mathbf{I}_1(\mathbf{x}))$  is diffuse component of  $\mathbf{I}_1(\mathbf{x})$ ,  $s(\mathbf{I}_1(\mathbf{x}))$  is specular component of  $\mathbf{I}_1(\mathbf{x})$  and  $\Omega_1$  is region in  $\mathbf{I}_1(\mathbf{x})$  where object is depicted. Data structure for  $\mathbf{A}$  and  $\mathbf{B}$  stores pairs of the dot product and color. For each pixel coordinates  $\mathbf{x}$  of the object in the material image, the dot product  $\mathbf{N}_1(\mathbf{x}) \cdot \mathbf{L}_1$  and the diffuse component  $d(\mathbf{I}_1(\mathbf{x}))$  are stored into  $\mathbf{A}$ . Similarly, for each pixel coordinates  $\mathbf{x}$  of the object in material image the dot product  $\mathbf{N}_1(\mathbf{x}) \cdot \mathbf{H}_1$  and its corresponding specular component  $s(\mathbf{I}_1(\mathbf{x}))$  are stored into  $\mathbf{B}$ .

Transfer of the material appearance is achieved by changing pixels colors of the object in  $\mathbf{I}_2(\mathbf{x})$ . For each pixel coordinate  $\mathbf{x}$  of the object in  $\mathbf{I}_2(\mathbf{x})$  we determine the  $\hat{d}(\mathbf{x})$  and  $\hat{s}(\mathbf{x})$ . We select two elements  $(a_1, c_1)$  and  $(a_2, c_2)$  from  $\mathbf{A}$ . The first element  $(a_1, c_1)$  where  $a_1 = \max\{a \mid a \geq \mathbf{N}_2(\mathbf{x}) \cdot \mathbf{L}_2, (a, c) \in \mathbf{A}\}$  is the pair which has first component closest upper to  $\mathbf{N}_2(\mathbf{x}) \cdot \mathbf{L}_2$  while the second element  $(a_2, c_2)$  where  $a_2 = \min\{a \mid a \leq \mathbf{N}_2(\mathbf{x}) \cdot \mathbf{L}_2, (a, c) \in \mathbf{A}\}$  has its dot product component closest lower to  $\mathbf{N}_2(\mathbf{x}) \cdot \mathbf{L}_2$ . The color  $\hat{d}(\mathbf{x})$  is then defined as the linear interpolation of the color components  $c_1$  and  $c_2$ . The color  $\hat{s}(\mathbf{x})$  is defined as the linear interpolation of color components  $c_3$  and  $c_4$  of two elements  $(b_1, c_3)$  and  $(b_2, c_4)$  from  $\mathbf{B}$ ,  $b_1 = \max\{b \mid b \leq \mathbf{N}_2(\mathbf{x}) \cdot \mathbf{H}_2, (b, c) \in \mathbf{B}\}$  and  $b_2 = \min\{b \mid b \geq \mathbf{N}_2(\mathbf{x}) \cdot \mathbf{H}_2, (b, c) \in \mathbf{B}\}$ , respectively. Then pixel color of the object at coordinates  $\mathbf{x}$  in the original image is changed as follows:

$$\mathbf{I}_2(\mathbf{x}) = \hat{d}(\mathbf{x}) + \hat{s}(\mathbf{x}). \quad (6.9)$$

#### 6.1.4 Results

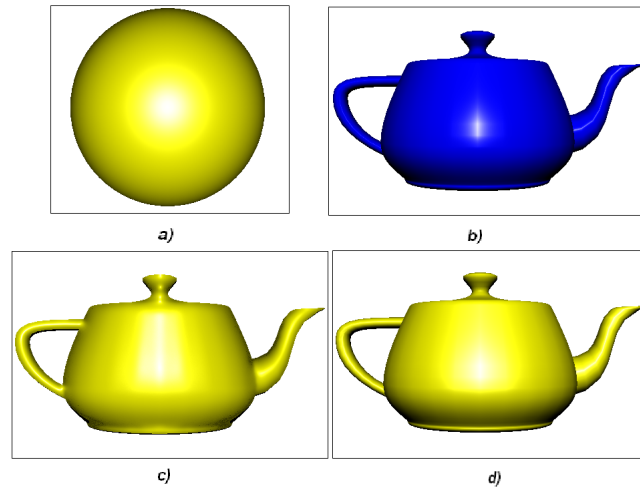
Proposed method was tested on multiple synthetic images using Phong and Cook–Torrance illumination model. Best result has been obtained in the material image  $\mathbf{I}_1(\mathbf{x})$  with a single sphere and with the same light and viewer direction.

Figure 6.4 shows a material appearance transfer from the yellow sphere with the shininess coefficient 30 to the blue teapot with the shininess coefficient 100. The direction of the light in case of the sphere was  $(0, 0, 1)$  and estimation was  $\mathbf{L}_1 = (-0.002, -0.001, 1)$ . In the case of the teapot the light direction was  $(0, -0.4, 1)$  and the estimation of the light direction was  $\mathbf{L}_2 = (-0.02, -0.18, 0.983)$ . Inaccuracies in normal estimations was affected by errors in the light direction estimations of the Zheng & Chellappa’s method.

Figure 6.5 shows the result of the appearance transfer from the sphere with the metallic car painting to the yellow teapot. Estimation of  $\mathbf{L}_1 = (-0.16, -0.136, 0.98)$  and  $\mathbf{L}_2 = (-0.0768, 0.252, 0.96)$ . The Horn and Brooks algorithm tends to over smooth the recovered normal map, which leads to losing of the boundaries. The problem of improper estimation of the geometry of the object in the material image  $\mathbf{I}_1(\mathbf{x})$  leads to certain noise in the result. This noise is due to errors in the recovered normal map which leads to the constructions of structures  $\mathbf{A}$  and  $\mathbf{B}$ , where some element may have the dot product component higher then some other elements, but the color components consists of the color with lower intensity.

Figure 6.6 shows transfer of the metallic material to the car bonnet. Average relative error of the pixels of the bonnet region in our resulting image compared with rendered image was 14.837% of the transfer depicted in first row and 11.989% in second row.

The bottleneck of this method is the inaccuracy of the classic shape from shading algorithms. There can be some improvement accomplished by involving a user interaction to the shape recovering process as proposed in [91]. An attempt to decrease the dependency on the shape from shading algorithm of the proposed appearance transformation method may



**Figure 6.4:** *Material transfer from yellow sphere to the teapot. a) The material image  $\mathbf{I}_1(\mathbf{x})$ . b) The object image  $\mathbf{I}_2(\mathbf{x})$ . c) The material appearance of the object in  $\mathbf{I}_1(\mathbf{x})$  transferred to the object in  $\mathbf{I}_2(\mathbf{x})$ . d) The original object from  $\mathbf{I}_2(\mathbf{x})$  rendered with the same material and scene parameters as the parameters of the object in  $\mathbf{I}_1(\mathbf{x})$ .*

also increase the accuracy. Another improvement of the proposed method may be achieved by generalisation of the assumption of the illumination and the object's surface composition. Incorporating an environment map analysis may allow appearance transformation of the material surface which reflects surroundings.

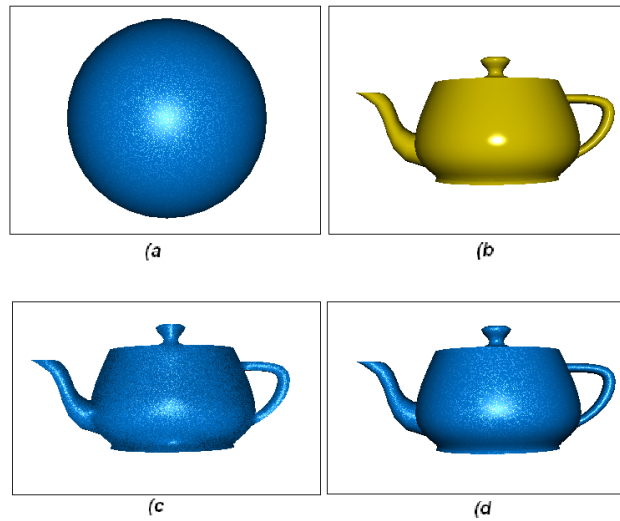


**Figure 6.5:** *Transferring sparkling material from the sphere to the teapot. a) The material image  $\mathbf{I}_1(\mathbf{x})$ . b) The object image  $\mathbf{I}_2(\mathbf{x})$ . c) The material appearance of the object in  $\mathbf{I}_1(\mathbf{x})$  transferred to the object in  $\mathbf{I}_2(\mathbf{x})$ . d) The original object from  $\mathbf{I}_2(\mathbf{x})$  rendered with the same material and scene parameters as the parameters of the object in  $\mathbf{I}_1(\mathbf{x})$ .*

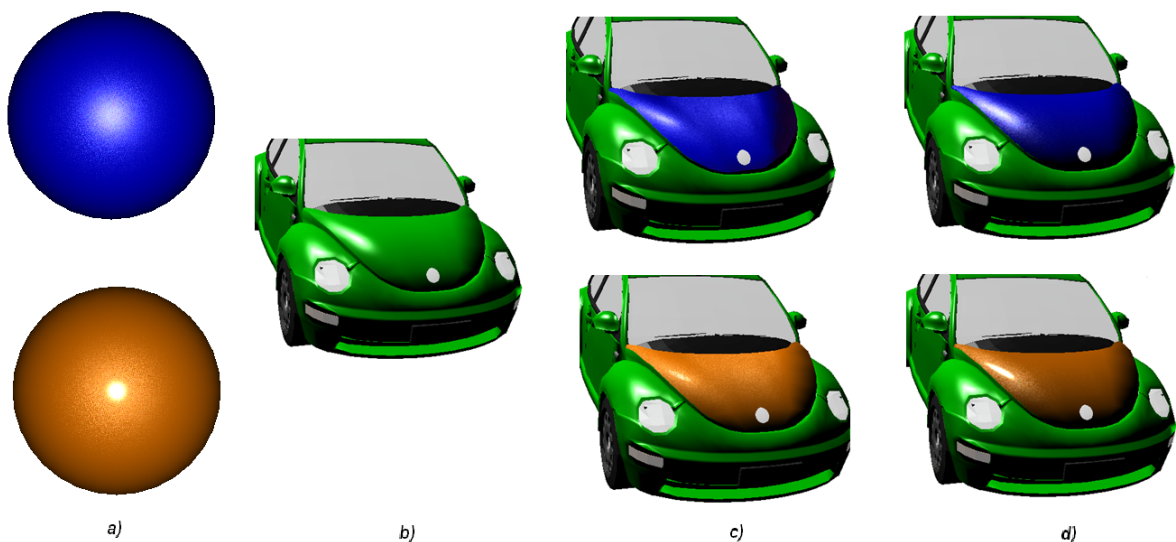


**Figure 6.6:** *a) Source images. b) The target image. c) Source material applied onto the bonnet of the car. d) Bonnets rendered with the same material parameters as the parameters of the object in source images.*

# Bibliography

- [1] ACHUTHA, S. Brdf acquisition with basis illumination. Master's thesis, Department of Computer Science, University of British Columbia, Vancouver, Canada, 2006.
- [2] A.GÜLTEKIN, AND GÖKMEN, M. Adaptive shape from shading. In *Proc. of the Eleventh International Symposium on Computer and Information Sciences (ISCIS XI)* (Turkey, 1996), pp. 83–92.
- [3] BELLAIRE, G., AND SCHLÜNS, K. 3-d object recognition by matching the total view information. In *ICPR '96: Proceedings of the 1996 International Conference on Pattern Recognition (ICPR '96) Volume I* (Washington, DC, USA, 1996), IEEE Computer Society, p. 534.
- [4] BEN-EZRA, M., WANG, J., WILBURN, B., LI, X., AND MA, L. An LED-only brdf measurement device. In *CVPR (2008)*, IEEE Computer Society.
- [5] BLINN, J. F. Models of light reflection for computer synthesized pictures. *SIGGRAPH Comput. Graph.* 11, 2 (1977), 192–198.
- [6] BOIVIN, S., AND GAGALOWICZ, A. Image-Based Rendering from a Single Image. Research Report RR-4098, INRIA, 2001.
- [7] BOIVIN, S., AND GAGALOWICZ, A. Image-based rendering of diffuse, specular and glossy surfaces from a single image. In *SIGGRAPH '01: Proceedings of the 28th annual conference on Computer graphics and interactive techniques* (New York, NY, USA, 2001), ACM, pp. 107–116.
- [8] BROOKS, M. J., AND HORN, B. K. P. Shape and source from shading. *Shape from shading* (1989), 53–68.
- [9] COOK, R. L., AND TORRANCE, K. E. A reflectance model for computer graphics. *ACM Trans. Graph.* 1, 1 (1982), 7–24.
- [10] ČUTRÍKOVÁ, M. Popis ľudského vnímania lesku, Bachelor's thesis, Department of applied informatics, faculty of natural sciences, University of Saint Cyril and Metod, 2009.
- [11] DEBEVEC, P. Rendering synthetic objects into real scenes: bridging traditional and image-based graphics with global illumination and high dynamic range photography. In *SIGGRAPH '98: Proceedings of the 25th annual conference on Computer graphics and interactive techniques* (New York, NY, USA, 1998), ACM, pp. 189–198.
- [12] DEMPSKI, K., AND VIALE, E. *Advanced Lighting and Materials with Shaders*. Wordware Publishing, Inc., Plano, Texas, USA, 2005.
- [13] DORSEY, J., RUSHMEIER, H., AND SILLION, F. *Digital Modeling of Material Appearance*. Morgan Kaufmann, San Francisco, USA, 2008.

- [14] DOWLING, J. E. *The Retina: An Approachable Part of the Brain*. The Belknap Press of Harvard University Press, Cambridge, Massachusetts, USA, 1987.
- [15] DREW, M. S., AND KONTSEVICH, L. L. Closed-form attitude determination under spectrally varying illumination. In *In Proc. IEEE Comp. Soc. Conf. on* (1994), pp. 985–990.
- [16] DROR, R. O., ADELSON, E. H., AND WILLSKY, A. S. Recognition of surface reflectance properties from a single image under unknown real-world illumination. In *Proc. of the IEEE Workshop on Identifying Objects Across Variations in Lighting* (2001), MIT CSAIL.
- [17] ĎURIKOVIČ, R. Explicit method of sparkling effect simulation. *Journal of Three Dimensional Images* 16, 4 (2002), 96–100.
- [18] ĎURIKOVIČ, R. Appearance measurements in industry and their application in light reflection models. *Journal of Three Dimensional Images* 21, 1 (2007), 47–52.
- [19] ĎURIKOVIČ, R., AND ÁGOŠTON, T. Prediction of optical properties of paints. *Central European Journal of Physics* 5, 3 (2007), 416–427.
- [20] ĎURIKOVIČ, R., AND KIMURA, R. GPU rendering of the thin film on paints with full spectrum. *International Conference on Information Visualisation* (2006), 751–756.
- [21] ĎURIKOVIČ, R., KOLCHIN, K., AND ERSHOV, S. Rendering of japanese artcraft. In *Short Presentations of EUROGRAPHICS Conference* (Braunschweig, Germany, 2002), pp. 131–138.
- [22] ĎURIKOVIČ, R., AND ŠEĎO, I. Real-time friendly representation of arbitrary brdf with appearance industry measurements. *Journal of the Applied Mathematics, Statistics and Informatics* 3, 1 (2007), 17–26.
- [23] EBNER, M. *Color Constancy*. John Wiley & Sons, Inc., New York, NY, USA, 2007.
- [24] ERSHOV, S., ĎURIKOVIČ, R., KOLCHIN, K., AND MYSZKOWSKI, K. Reverse engineering approach to appearance-based design of metallic and pearlescent paints. *Vis. Comput.* 20, 8-9 (2004), 586–600.
- [25] ERSHOV, S., KOLCHIN, K., AND MYSZKOWSKI, K. Rendering pearlescent appearance based on paint-composition modelling. *Computer Graphics Forum* 20, 3 (2001), 221–238.
- [26] FILIN, M. Priemyselné merania vzhľadu a štatistické vyhodnocovanie, Bachelor’s thesis, Department of applied informatics, faculty of natural sciences, University of Saint Cyril and Metod, 2009.
- [27] FLEMING, B. *Advanced 3D photorealism techniques*. John Wiley & Sons, Inc., New York, NY, USA, 1999.
- [28] FOLEY, J. D., VAN DAM, A., FEINER, S. K., AND HUGHES, J. F. *Computer Graphics: Principles and Practice. Second Edition in C*. Addison-Wesley Publishing Company, Massachusetts, USA, 1996.
- [29] GONDEK, J. S., MEYER, G. W., AND NEWMAN, J. G. Wavelength dependent reflectance functions. In *SIGGRAPH ’94: Proceedings of the 21st annual conference on Computer graphics and interactive techniques* (New York, NY, USA, 1994), ACM, pp. 213–220.

- [30] GÜNTHER, J., CHEN, T., GOESELE, M., WALD, I., AND SEIDEL, H.-P. Efficient acquisition and realistic rendering of car paint. In *Proceedings of 10th International Fall Workshop - Vision, Modeling, and Visualization (VMV) 2005* (Nov. 2005), G. Greiner, J. Hornegger, H. Niemann, and M. Stamminger, Eds., Akademische Verlagsgesellschaft Aka GmbH, pp. 487–494.
- [31] HE, X. D., TORRANCE, K. E., SILLION, F. X., AND GREENBERG, D. P. A comprehensive physical model for light reflection. *SIGGRAPH Comput. Graph.* 25, 4 (1991), 175–186.
- [32] HORN, B. Obtaining shape from shading information. In *The Psychology of Machine Vision* (New York, NY, USA, 1975), McGraw-Hill, pp. 115–155.
- [33] HORN, B. K. P. *Robot Vision*. The MIT Press, Massachusetts, USA, 1986.
- [34] HORN, B. K. P., AND BROOKS, M. J. The variational approach to shape from shading. *Comput. Vision Graph. Image Process.* 33, 2 (1986), 174–208.
- [35] HUNTER, R. S. Methods of determining gloss. *Journal of Research* 18, I (1937), 19–39.
- [36] HUNTER, R. S., AND HAROLD, R. W. *The Measurement of Appearance*. John Wiley & Sons, Inc., New York, NY, USA, 1987.
- [37] JAMES A. FERWERDA, F. P., AND GREENBERG, D. P. A psychophysically-based model of surface gloss perception. In *Proceedings SPIE Human Vision and Electronic Imaging '01* (2001), pp. 291–301.
- [38] K. J. YOON, Y. J. C., AND KWEON, I. S. Fast separation of reflection components using a specularly-invariant image representation. In *IEEE International Conference on Image Processing (ICIP)* (2006), pp. 973–976.
- [39] KIM, D. B., KIM, K. Y., PARK, K. S., SEO, M. K., AND LEE, K. H. A fast and accurate image-based measuring system for isotropic reflection materials. Z.-H. Gu and L. M. Hanssen, Eds., vol. 7065, SPIE, p. 70650I.
- [40] KIMMEL, R., AND BRUCKSTEIN, A. M. Global shape from shading. *Comput. Vis. Image Underst.* 62, 3 (1995), 360–369.
- [41] KLINKER, G., SHAFER, S., AND KANADE, T. The measurement of highlights in color images. *International Journal of Computer Vision* 2, 1 (June 1988), 7–32.
- [42] KLINKER, G. J., SHAFER, S., AND KANADE, T. Image segmentation and reflection analysis through color. In *SPIE Applications of Artificial Intelligence VI* (1988), vol. 937, pp. 229–244.
- [43] L., V. H. P., AND J., C. M. An iterative multi-resolution shape-from-shading algorithm and its application to planetary mapping. In *International geoscience and remote sensing symposium* (1986), PAYS-BAS, pp. 1011–1016.
- [44] LAWRENCE, J., BEN-ARTZI, A., DECORO, C., MATUSIK, W., PFISTER, H., RAMAMOORTHY, R., AND RUSINKIEWICZ, S. Inverse shade trees for non-parametric material representation and editing. *ACM Trans. Graph.* 25, 3 (2006), 735–745.
- [45] LEE, C. H., AND ROSENFELD, A. Improved methods of estimating shape from shading using the light source coordinate system. *Artif. Intell.* 26, 2 (1985), 125–143.
- [46] MALLICK, S., ZICKLER, T., KRIEGMAN, D., AND BELHUMEUR, P. Beyond lambert: Reconstructing specular surfaces using color. In *IEEE Computer Society Conference on Computer Vision and Pattern Recognition* (2005), vol. 2, pp. 619–626.

- [47] MATUSIK, W., PFISTER, H., BRAND, M., AND McMILLAN, L. A data-driven reflectance model. In *SIGGRAPH '03: ACM SIGGRAPH 2003 Papers* (New York, NY, USA, 2003), ACM, pp. 759–769.
- [48] MEYER, G. W., SHIMIZU, C., EGGLEY, A., FISCHER, D., KING, J., AND RODRIGUEZ, A. Computer aided design of automotive finishes. In *Proceedings of AIC Colour 05* (2005), pp. 685–688.
- [49] MIHÁLIK, A. Algorithm design for real-time rendering of the natural waters. Master's thesis, Faculty of Mathematics, Physics and Informatics, Comenius University, Bratislava, Slovakia, 2008.
- [50] MIHÁLIK, A., AND ĎURIKOVIČ, R. Appearance transformation of 3d objects depicted in images. In *International Conference on Applied Natural Sciences ANS 2009* (Trnava, Slovakia, 2009), Faculty of Natural Sciences UCM Press, p. 95 (book of abstracts).
- [51] MIHÁLIK, A., AND ĎURIKOVIČ, R. Material appearance transfer between images. In *Proceedings of the Spring Conference on Computer Graphics - SCCG2009, Budmerice, Slovakia* (2009), 55–58.
- [52] NASSAU, K. *The Physics and Chemistry of Color: The Fifteen Causes of Color*. John Wiley & Sons, Inc., New York, NY, USA, 2001.
- [53] NOVAK, C. L., AND SHAFER, S. A. Estimating scene properties from color histograms. Tech. rep., Pittsburgh, PA, USA, 1992.
- [54] ONONYE, A., AND SMITH, P. Estimating the shape of a surface with non-constant reflectance from a single color image. In *Proceedings of the British Machine Vision Conference 2002* (2002), pp. 163–172.
- [55] OREN, M., AND NAYAR, S. K. Generalization of lambert's reflectance model. In *SIGGRAPH 94* (1994), ACM Press, pp. 239–246.
- [56] PELLACINI, F., FERWERDA, J. A., AND GREENBERG, D. P. Toward a psychophysically-based light reflection model for image synthesis. In *SIGGRAPH '00: Proceedings of the 27th annual conference on Computer graphics and interactive techniques* (New York, NY, USA, 2000), ACM Press/Addison-Wesley Publishing Co., pp. 55–64.
- [57] PELLACINI, F., AND LAWRENCE, J. Appwand: editing measured materials using appearance-driven optimization. In *SIGGRAPH '07: ACM SIGGRAPH 2007 papers* (New York, NY, USA, 2007), ACM, p. 54.
- [58] PENTLAND, A. P. Finding the illuminant direction. *JOSA* 72, 4 (1982), 448–455.
- [59] PHONG, B. T. Illumination for computer generated pictures. *Commun. ACM* 18, 6 (1975), 311–317.
- [60] PRADOS, E., AND FAUGERAS, O. Shape from shading. In *Mathematical Models in Computer Vision: The Handbook* (Warren, MI, USA, 2005), Springer.
- [61] PRADOS, E., AND FAUGERAS, O. Shape from shading: a well-posed problem ?, jun 2005.
- [62] R. ĎURIKOVIČ, S. ERSHOV, K. K., AND MYZKOWSKI, K. Solution of an inverse problem in rendering metallic and pearlescent appearance. In *Proceedings of the Human and Computer Conference - HC2004* (2004), pp. 52–58.

- [63] RAGHEB, H., AND HANCOCK, E. R. Separating lambertian and specular reflectance components using iterated conditional modes. In *Proc. British Machine Vision Conference* (2001), pp. 541–552.
- [64] REINHARD, E., WARD, G., PATTANAİK, S., AND DEBEVEC, P. *High Dynamic Range Imaging: Acquisition, Display, and Image-Based Lighting*. Morgan Kaufmann, San Francisco, USA, 2005.
- [65] ROBLES-KELLY, A., AND HANCOCK, E. R. Estimating the surface radiance function from single images. *Graph. Models* 67, 6 (2005), 518–548.
- [66] RON, G., AND PELEG, S. Multiresolution shape from shading. In *IEEE Computer Society Conference on Computer Vision and Pattern Recognition* (1989), pp. 350–355.
- [67] RON O. DROR, E. H. A., AND WILLSKY, A. S. Estimating surface reflectance properties from images under unknown illumination. In *Proc. SPIE* (2001), vol. 4299, pp. 231–242.
- [68] RUMP, M., MÜLLER, G., SARLETTE, R., KOCH, D., AND KLEIN, R. Photo-realistic rendering of metallic car paint from image-based measurements. *Computer Graphics Forum* 27, 2 (Apr. 2008).
- [69] RUŽCKÝ, E., AND FERKO, A. *Počítačová Grafika*. SAPIENTIA, Bratislava, Slovakia, 1995.
- [70] SATO, Y., WHEELER, M. D., AND IKEUCHI, K. Object shape and reflectance modeling from observation. 95–116.
- [71] SCHLÜNS, K., AND TESCHNER, M. Fast separation of reflection components and its application in 3d shape recovery. In *Proc. 3rd Color Imaging Conference* (Springfield, VA, USA, 1995), IS&T, pp. 48–51.
- [72] SERGEY V. ERSHOV, ANDREI B. KHODULEV, K. V. K. Simulation of sparkles of metallic paints. In *Proceeding of Graphicon* (1999), pp. 121–128.
- [73] SHAFER, S. A. Using color to separate reflection components. *Color Research & Application* 10, 4 (1985), 210–218.
- [74] SNYDER, W. C., WAN, Z., AND LI, X. Thermodynamic constraints on reflectance reciprocity and Kirchoff’s law. *Applied Optics* 37, 16 (1998), 3464–3470.
- [75] SU XUEY, JIAPING WANG, X. T. Q. D., AND GUO, B. Image-based material weathering. *Computer Graphics Forum* 27, 2 (2008), 617–626.
- [76] TAKAGI, A., TAKAOKA, H., OSHIMA, T., AND OGATA, Y. Accurate rendering technique based on colorimetric conception. In *SIGGRAPH ’90: Proceedings of the 17th annual conference on Computer graphics and interactive techniques* (New York, NY, USA, 1990), ACM, pp. 263–272.
- [77] TAN, P., QUAN, L., AND LIN, S. Separation of highlight reflections on textured surfaces. In *CVPR ’06: Proceedings of the 2006 IEEE Computer Society Conference on Computer Vision and Pattern Recognition* (Washington, DC, USA, 2006), IEEE Computer Society, pp. 1855–1860.
- [78] TAN, R. T., AND IKEUCHI, K. Reflection components decomposition of textured surfaces using linear basis functions. *Computer Vision and Pattern Recognition, IEEE Computer Society Conference on 1* (2005), 125–131.

- [79] TAN, R. T., AND IKEUCHI, K. Separating reflection components of textured surfaces using a single image. *IEEE Trans. Pattern Anal. Mach. Intell.* 27, 2 (2005), 178–193.
- [80] TAN, R. T., NISHINO, K., AND IKEUCHI, K. Color constancy through inverse-intensity chromaticity space. *J. Optical Society of America A* 21, 3 (2004), 321–334.
- [81] TOMINAGA, S., AND TANAKA, N. Estimating reflection parameters from a single color image. *IEEE Comput. Graph. Appl.* 20, 5 (2000), 58–66.
- [82] TOMINAGA, S., AND WANDELL, B. A. Natural scene–illuminant estimation using the sensor correlation. In *Proceedings of the IEEE* (New York, NY, USA, 2002), Institute of Electrical and Electronics Engineers, pp. 42–56.
- [83] TORRANCE, K. E., AND SPARROW, E. M. Theory for off-specular reflection from roughened surfaces. *JOSA* 57, 9 (1967), 1105–1114.
- [84] TSAI, P. S., AND SHAH, M. Shape from shading using linear approximation. *Image and Vision Computing* 12, 8 (1994), 487–498.
- [85] ĀURIKOVIČ, R., AND MARTENS, W. L. Simulation of sparkling and depth effect in paints. In *SCCG '03: Proceedings of the 19th spring conference on Computer graphics* (New York, NY, USA, 2003), ACM, pp. 193–198.
- [86] WANG, J., TONG, X., LIN, S., PAN, M., WANG, C., BAO, H., GUO, B., AND SHUM, H.-Y. Appearance manifolds for modeling time-variant appearance of materials. *ACM Trans. Graph.* 25, 3 (2006), 754–761.
- [87] WARD, G. J. Measuring and modeling anisotropic reflection. *SIGGRAPH Comput. Graph.* 26, 2 (1992), 265–272.
- [88] WESTLUND, H. B., AND MEYER, G. W. Applying appearance standards to light reflection models. In *SIGGRAPH '01: Proceedings of the 28th annual conference on Computer graphics and interactive techniques* (New York, NY, USA, 2001), ACM, pp. 501–51.
- [89] WOLFF, L. B., NAYAR, S. K., AND OREN, M. Improved diffuse reflection models for computer vision. *Int. J. Comput. Vision* 30, 1 (1998), 55–71.
- [90] WORTHINGTON, P. L., AND HANCOCK, E. R. New constraints on data-closeness and needle map consistency for shape-from-shading. *IEEE Trans. Pattern Anal. Mach. Intell.* 21, 12 (1999), 1250–1267.
- [91] YASUYUKI, G. Z., ZENG, G., MATSUSHITA, Y., QUAN, L., AND YEUNG SHUM, H. Interactive shape from shading. In *IEEE Proceedings of Computer Vision and Pattern Recognition* (1999), pp. 343–350.
- [92] YU, Y., DEBEVEC, P., MALIK, J., AND HAWKINS, T. Inverse global illumination: recovering reflectance models of real scenes from photographs. In *SIGGRAPH '99: Proceedings of the 26th annual conference on Computer graphics and interactive techniques* (New York, NY, USA, 1999), ACM Press/Addison-Wesley Publishing Co., pp. 215–224.
- [93] ZHANG, R., TSAI, P.-S., CRYER, J. E., AND SHAH, M. Shape from shading: A survey. *IEEE Trans. Pattern Anal. Mach. Intell.* 21, 8 (1999), 690–706.
- [94] ZHENG, Q., AND CHELLAPA, R. Estimation of illuminant direction, albedo, and shape from shading. *IEEE Transactions on Pattern Analysis and Machine Intelligence* 13 (1991), 680–702.

# Publications

- [1] Andrej Mihálik and Roman Ďurikovič. Natural Water Shared. In *SCCG '08: Proceedings of the Spring Conference on Computer Graphics*, pages 23–26, Budmerice, Slovakia, 2008.
- [2] Andrej Mihálik. Algorithm Design for Real-Time Rendering of the Natural Waters. Master's thesis, Faculty of Mathematics, Physics and Informatics, Comenius University, Bratislava, Slovakia, 2008.
- [3] Andrej Mihálik and Roman Ďurikovič. Material Appearance Transfer Between Images. In *SCCG '09: Proceedings of the Spring Conference on Computer Graphics*, pages 55–58, Budmerice, Slovakia, 2009.
- [4] Andrej Mihálik and Roman Ďurikovič. Appearance Transformation of 3D Objects Depicted in Images. In book of abstracts of the International Conference on Applied Natural Sciences ANS 2009, page 95, 2009.